Discontinuous Galerkin Time Domain Methods in Computational Electrodynamics: State of the Art

L. D. Angulo, J. Alvarez, M. F. Pantoja, S. G. Garcia, and A. R. Bretones

***Abstract*—This text reviews the state of the art of the Discontinuous Galerkin (DG) method applied to the solution of the Maxwell's equations in Time Domain (TD). The work is divided into two parts. In the first part, the mathematical formulation of the DGTD method, together with a review and a discussion on the different ways to implement it is presented. The second part presents models and techniques to address usual needs in electromagnetic simulations such as plane wave illumination, local electromagnetic sources, wave port modeling, dispersive and/or anisotropic materials and sub-cell models, including lumped elements, thin layers, surface impedances, and thin wires.**

***Index Terms*—Discontinuous Galerkin Methods, Maxwell's equations, Computational Electromagnetics**

I. Introduction

In the last years Discontinuous Galerkin time-domain (DGTD) techniques have reached a significant level of maturity demonstrating their capability of obtaining highly accurate results at an affordable computational cost. They have successfully been used to solve many kinds of differential equations in fields including: Computational Fluid Dynamics [1], Magnetohydrodynamics [2], Quantum mechanics [3], and Elastodynamics [4], [5]. In this paper, we will review some of the existing DGTD techniques with special emphasis on applications to Computational Electromagnetics (CEM).

The DG spatial discretization permits us to take advantage of using unstructured high-order finite elements. This allows an accurate discretization of the geometry using different sizes and types of cells (h-adaptivity), and also to obtain high-order convergence of the electromagnetic (EM) solution depending on the order of basis functions within each cell (p-adaptivity). The TD nature of this method, compared to its frequency-domain (FD) counterpart, offers benefits in several kinds of EM problems such as those where we need to study a transient field effect of an arbitrary time-signal excitation (e.g. lightning strikes, EMC coupling, ultra-wideband antennas), or the non-linear behavior of materials, components or networks, where TD offers a direct and efficient approach. To solve these problems, we have developed a solver: SEMBA (Simulador Electromagnetico de Banda Ancha) [6]. SEMBA implements many of the techniques that are reviewed in this text such as vector/nodal basis, centered/penalized/upwind fluxes, special materials, Local Time Stepping (LTS) techniques, hp-adaptivity, and OpenMP/MPI parallelization. These techniques have been thoroughly tested in a wide range of problems, demonstrating to provide robust and efficient solutions [7]–[23].

However, the aim of this paper is not restricted to describing only those techniques directly tested by ourselves, but also to make a full review of the state-of-the-art including contributions found in the most recent literature. The rest of this work is divided into three parts: The first part (Sections II and III) provides a general review of the state-of-the-art. The second part (Sections IV and V) describes the mathematical foundation of the method, alternative introductory texts on this topic are [24]–[26]. Much of what is done in this part can be generalized to other partial differential equations (PDEs). The third part of this work (Sections VI, VII, VIII, and IX) is focused on the application of this method to real engineering problems. Several techniques to simulate electromagnetic sources, special materials (such as dispersive and anisotropic), and sub-cell models are introduced. Another text discussing some of these topics is [27].

II. Overview of time-domain numerical methods

Let us start by situating DGTD in the context of some of the most common TD full-wave numerical methods used in CEM. Their main typical features are summarized in table I.

A. Finite Differences in Time Domain (FDTD)

FDTD is a mature technique that has been extensively developed for over 50 years. The classical FDTD method [33] employs a second order finite centered approximation for space and time derivatives in Maxwell's curl equations. This technique places the samples of the electric field in a rectilinear Cartesian grid while the magnetic field is sampled in the dual of this grid, resulting in what is known as the Yee's cell [34]. The fields are then advanced in a marching-on-in-time fashion using a second order leap-frog (LF2) algorithm. The final scheme is second order convergent with respect to spatial and temporal refinement.

The main advantages of the FDTD method are its computational efficiency, its naturally spurious-free solutions and the fact that it conserves energy. On the other hand, the need of a rectilinear grid and the staggering of the fields sampling imply a high degeneration of the geometrical information due to staircasing effects. However, the FDTD method can be used together with geometrically conformal [29] or subgridding [30] techniques that alleviate this limitation. Higher-order FDTD techniques can be formulated, but they require a larger

The $1^{st}, 3^{rd}, 4^{th}$, and 5^{th} authors are with the Dept. of Electromagnetism, Univ. Granada, 18071 Granada, Spain, (Corresponding: lmdiazangulo@ugr.es). The 2^{nd} is with Airbus Defense and Space, 28906 Getafe, Spain.

TABLE I: Comparative summary of numerical methods with typical formulations

	FDTD	FVTD	DGTD	FEMTD (others)
Order of accuracy[a] [b]	$h^{2,c}$	h	h^{2p+1}	h^{2p}
Geometry adaptivity	No[d]	Yes	Yes	Yes
Spurious modes	No	Yes/No	Yes[e]/No[f]	Yes[g]/No[h]
Energy conservative[b]	Yes	Yes	Yes[e]/No[f]	Yes
Explicit form	Yes	Yes	Yes	No[i]
LTS, IMEX or similar	No	Yes	Yes	No
Parallel. simplicity	High	High	High	Low
Memory usage[j]	High	Very High	Low	Very Low
Memory locality	Very High	Low	High[k]	High[k]
Uses dual mesh	Yes	No	No[l]	No
Allows non-conformal mesh	No	Yes	Yes	No
h adaptivity	Yes	Yes	Yes	Yes
p adaptivity	No	No	Yes	Yes

[a]For global L^2 norm.
[b]Considering spatial semi-discretization only.
[c]Higher order spatial semi-discretizations are also available [28].
[d]Can be alleviated with conformal [29] and subgridding [30] techniques.
[e]With centered fluxes.
[f]With penalized fluxes.
[g]For nodal basis
[h]For vector basis.
[i]But can be approximated [31].
[j]For a structured mesh. Not considering semi-discretized operators.
[k]For high orders.
[l]Improvements using a dual mesh have been reported by [32].

stencil [28], [35], [36] that reduces significantly its computational efficiency. The Finite Integration Technique (FIT) and the Transmission Line Method (TLM) are closely related to FDTD. FIT starts from Maxwell's curl equations in integral form and TLM from equivalent transmission-line equations. The resulting algorithms share most of the features that we find in the FDTD method.

B. Finite Volume Methods (FVTD)

The FVTD technique emerged as an alternative to FDTD aiming to overcome its geometrical discretization constraints, avoiding the staggered spatial discretization of the fields. The most common formulation of FVTD is carried on tetrahedral elements for the solution of Maxwell's curl equations [37]–[39]. The scheme is formulated by defining a system of equations in which the time derivative of the $\vec{E}$ fields integrated in volume equals to the sum of all surface integrals of the spatial derivative of $\vec{H}$ terms and vice versa. The spatial semi-discretization is then evolved, similarly to the FDTD method, using an LF2 algorithm. The main drawback of FVTD is that its order of convergence is 1 [40], which is quite low. Moreover, the timestep is limited by a condition that depends on the shape of the elements which is more restrictive than for the FDTD method. A way to mitigate this time-stepping constraint is to use local time stepping (LTS) techniques [37]. LTS can also be used for DGTD as we will describe in Section V. FVTD can be formally seen as a zero-order DGTD method.

C. Finite Element Methods (FEMTD)

A variety of time-domain FEM schemes has been proposed [41] based on Maxwell's curl-curl equation or the hyperbolic system of curl equations (Ampere's and Faraday's laws). The second-order vector-wave curl-curl equation, typically solved by FEM in FD, can also be solved by FEM in TD [42]–[51] requiring only the computation of a single field (electric or magnetic). Its major drawback is that a global linear system of equations needs to be solved at each timestep. To reduce the number of timesteps, unconditionally implicit time-integration schemes, such as Newmark-beta can be used, at the expense of yielding quite ill-conditioned matrices [52].

Alternatives to the single-field scheme are found by employing the two first-order coupled Maxwell's curl equations, either formulated by considering the electric field intensity $\vec{E}$ and the magnetic flux density $\vec{B}$ (E-B), or the electric field intensity $\vec{E}$ and magnetic field intensity $\vec{H}$ (E-H). These formulations offer certain advantages with respect to the single-field formulation, such as the possibility of using different expansion functions and avoiding spurious solutions. Moreover, the first-order time derivatives allow the use of a conventional LF2 time-integration method, eliminating the need of saving previous states in memory. However, because of the tangential-continuity condition, they still require solving a sparse linear system at each timestep, resulting in a computational cost comparable to that of the single-field scheme [53]–[58].

D. Discontinuous Galerkin Methods

A different family of FEM is found by relaxing the tangential-continuity condition, yielding the so-called discontinuous Galerkin methods (DGM). The continuity is imposed on numerical fluxes rather than on the tangential field components, in order to connect the solution between adjacent elements. The main advantage of DGM over other FEM methods in TD is the fact that the linear system to be solved becomes block-diagonal by requiring only a single inversion of K square matrices of $N \times N$ elements (with K the

number of elements and N the number of basis functions per element) which can be done at the pre-processing stage. One of the drawbacks is that the degrees of freedom (DOF) at the element interfaces are duplicated, a minor price considering the improvement in computational efficiency of the resulting explicit semi-discrete scheme [10], [19], [24], [59].

III. Applications of DGTD

The spectrum of engineering applications of CEM is extremely wide, giving rise to a need of different numerical methods as there is not an ever-suitable method capable of solving all types of real-world EM problems [60]. The following is a non-exhaustive list of some areas where DGTD methods can be of particular interest:

A. Multi-scale problems

Any problem exhibiting disparate sizes, such as IC packaging or in-place antenna simulations, can greatly benefit from a DGTD approach [20], [22], [26], [61], [62] combined with LTS and hp adaptivity techniques.

B. Electromagnetic Compatibility (EMC)

EMC problems are an increasingly big concern for the industry. Aircraft and car manufacturers perform CEM analysis to detect and solve possible EMC issues in eager stages of design. Simulations are usually performed to back measured data. However, sometimes measurements are difficult to perform, as in the case of lightning strikes or High-Intensity Radiated Fields (HIRF), and manufacturers have no other option than to rely exclusively on simulations. The degree of confidence put into these simulations is such that they have been allowed as valid tests for certification purposes [15], [63]. To perform EMC simulations, a DGTD code often must include models for sub-cell thin wires and composite layers (Section VIII) [14], [64], [65]. Moreover, these simulations are usually performed over electrically large problems and a high-performance and accuracy simulation is a requirement.

C. Antennas

An essential characteristic for the accurate simulation of wideband antenna systems is the modeling of their intricate geometrical details [12], [22]. In these kind of structures, an accurate modeling is critical in zones with small geometrical details, such as feeding ports. Frequency domain (FD) methods, such as the Method of Moments (MoM) or the Finite Element Method (FEM), are the usual choices for their capability of accurately modeling fine geometrical details. However, FD methods may become computationally inefficient for ultra-wideband analysis, since each frequency needs a complete simulation, typically involving a linear system resolution. Time-domain methods are a natural alternative for these purposes. Among them, DGTD methods are ideally suited for this purpose. LTS techniques, which are reviewed in Section V allow us to handle antenna geometries efficiently. Some techniques to model ports are described in section VI-C.

D. Waveguides

Like antennas, the simulation of waveguides usually needs the modeling of intricate geometries where DGTD offers an efficient solution. TD simulations allow us to estimate the resonant frequencies of these structures in a single run. Waveguides are usually resonant structures where the absence of spurious modes is a must [10], a discussion on how to keep spurious modes under control is carried out in Section IV-E. Moreover, the electromagnetic waves, often imping at grazing angles of incidence at the terminations of the waveguide. This makes necessary the use of an special treatment at the terminations, such as the use of Perfectly Matched Layers (PMLs) described in Section VII-A, or the multi-modal pseudo-analytical termination presented in [66].

E. Radar Cross Section

The analysis of the Radar Cross Section (RCS) of aircrafts can also be carried out with DGTD methods in an efficient manner [18], [20]. In this case, the TD nature allows us to efficiently perform monostatic RCS in a single run. The LTS technique, PMLs, Huygens sources (Section VI-A), and the ability to model complex geometries enables this task. A comparison with other numerical techniques is presented in [18] where, for a broadband solution, the DGTD method is demonstrated to be competitive with other methods classically used for this task, such as the MoM.

F. Ground Penetrating Radar (GPR)

GPR techniques can benefit from simulations when new antennas are being designed or complex geometries are under study. Simulations can be helpful in understanding in-the-field obtained data. Moreover, ground materials are usually dispersive and non-homogeneous. FEM and DGTD can model materials with gradually changing electrical properties in cells. Dispersive and lossy ground media can also be included [9], [67].

IV. The Discontinuous Galerkin Method

Maxwell's curl equations for lossless isotropic linear media without sources are

$$\mu \frac{\partial \vec{H}}{\partial t} = -\nabla \times \vec{E} \tag{1}$$

$$\varepsilon \frac{\partial \vec{E}}{\partial t} = \nabla \times \vec{H} \tag{2}$$

with ε and μ being, respectively, the electric permittivity and the magnetic permeability that we will assume to be homogeneous and isotropic for simplicity. Dispersive media are treated in Section VII-B.

A. The Galerkin method

Let us call Ω the region where we want to solve equations (1) and (2) applying a DG formalism. This region Ω is

tessellated with K non-overlapping elements V_k fully covering the computational domain Ω_K

$$\Omega \simeq \Omega_K = \bigcup_k^K V_k \tag{3}$$

For simplicity, we will suppress the subscripts k everywhere except in V_k, uniquely identifying the element where we are working. We assume that they can be inferred from the element where the Galerkin integrals are carried on. Within each element, the fields $\vec{E}(t,\vec{r})$ and $\vec{H}(t,\vec{r})$ are approximated by a projection over a set of N vector-basis functions

$$\mathcal{B} = \left\{\vec{\psi}_1(\vec{r}),\ \vec{\psi}_2(\vec{r}),\ \ldots\ \vec{\psi}_N(\vec{r})\right\} \tag{4}$$

The Galerkin problem consists of minimizing the inner product of the fields, projected over $\mathcal{B}$ with respect to each of the functions basis (4) within each element V_k, leading to formulate eqs. (1) and (2) in weak form as

$$\int_{V_k} \vec{\psi}_i \cdot \left[\mu \frac{\partial \vec{H}}{\partial t} + \nabla \times \vec{E}\right]\ dV = 0 \tag{5}$$

$$\int_{V_k} \vec{\psi}_i \cdot \left[\varepsilon \frac{\partial \vec{E}}{\partial t} - \nabla \times \vec{H}\right]\ dV = 0 \tag{6}$$

$$\text{with: } i = 1, \ldots N$$

Let us now explicitly write the approximation $\vec{E}$ and $\vec{H}$ as the projection over the same basis, $\mathcal{B}$. Thus

$$\vec{E} \simeq \vec{E}^h = \sum_j^N E_j^h(t)\vec{\psi}_j(\vec{r}) \doteq \vec{\boldsymbol{\psi}}^T \mathbf{E} \tag{7}$$

$$\vec{H} \simeq \vec{H}^h = \sum_j^N H_j^h(t)\vec{\psi}_j(\vec{r}) \doteq \vec{\boldsymbol{\psi}}^T \mathbf{H} \tag{8}$$

with

$$\vec{\boldsymbol{\psi}} = \left[\vec{\psi}_1, \ldots, \vec{\psi}_N\right]^T \tag{9}$$

$$\mathbf{E} = \left[E_1^h, \ldots, E_N^h\right]^T \tag{10}$$

$$\mathbf{H} = \left[H_1^h, \ldots, H_N^h\right]^T \tag{11}$$

Inserting (7) and (8) into (5) and (6) we obtain the Galerkin semi-discretization

$$\int_{V_k} \vec{\psi}_i \cdot \left[\mu \vec{\boldsymbol{\psi}}^T \frac{\partial \mathbf{H}}{\partial t} + (\nabla \times \vec{\boldsymbol{\psi}}^T)\mathbf{E}\right]\ dV = 0 \tag{12}$$

$$\int_{V_k} \vec{\psi}_i \cdot \left[\varepsilon \vec{\boldsymbol{\psi}}^T \frac{\partial \mathbf{E}}{\partial t} - (\nabla \times \vec{\boldsymbol{\psi}}^T)\mathbf{H}\right]\ dV = 0 \tag{13}$$

$$\text{with: } i = 1, \ldots N$$

The first terms of eq. (12) and (13) serve to introduce the mass matrix, $\mathcal{M}$,

$$[\mathcal{M}]_{ij} = \int_{V_k} \vec{\psi}_i(\vec{r}) \cdot \vec{\psi}_j(\vec{r})\ dV \tag{14}$$

The curl terms of eq. (12) and (13) result in the stiffness matrix, $\mathcal{S}$,

$$[\mathcal{S}]_{ij} = \int_{V_k} \vec{\psi}_i(\vec{r}) \cdot \nabla \times \vec{\psi}_j(\vec{r})\ dV \tag{15}$$

In the form stated in (12) and (13), we are not specifying how the tangential components of the fields within each element relate to each other. If we enforce the fields, $\vec{E}^h$ and $\vec{H}^h$ to be globally continuous, this technique is called the Continuous Galerkin Time Domain (CGTD) or FEMTD method. The approximated fields then fulfill in a strong way

$$\hat{n}_f \times \vec{E}_f^h = \hat{n}_f \times \vec{E}_f^{h+} \tag{16}$$

$$\hat{n}_f \times \vec{H}_f^h = \hat{n}_f \times \vec{H}_f^{h+} \tag{17}$$

where the superscript $+$ indicates the field neighboring the element across face f. The main drawback of the resulting algorithm is that it requires the solution of a large set of linear equations.

B. Numerical flux

The DG method [68] relies on enforcing the continuity of the numerical flux across face f rather than the field components as in (16). Using basic vector identities, the curl terms in (12) (and similarly in (13)) can also be expressed as

$$\begin{aligned}
&\int_{V_k} \vec{\psi}_i(\vec{r}) \cdot (\nabla \times \vec{E}_f^h)\ dV = \\
&= \int_{V_k} \nabla \cdot (\vec{E}_f^h \times \vec{\psi}_i)\ dV + \int_{V_k} (\nabla \times \vec{\psi}_i) \cdot \vec{E}_f^h\ dV \\
&= \oint_{\partial V_k} \vec{\psi}_i \cdot (\hat{n} \times \vec{E}_f^h)\ d(\partial V) + \int_{V_k} (\nabla \times \vec{\psi}_i) \cdot \vec{E}_f^h\ dV
\end{aligned} \tag{18}$$

where $\hat{n}$ is a unit vector pointing outwards the element. The first term of the RHS of Eq.18 $\left(\hat{n} \times \vec{E}_f^h\right)$ is substituted by the flux function across face f $\left(\hat{n} \times \vec{E}_f^{h,*}\right)$.

Therefore, instead of plugging (16) into (18) and then into (12) and (13), we define numerical values of the tangential fields on $\partial V_{(f,k)}$, henceforth called numerical fluxes, $\vec{E}_f^{h,*}$ and $\vec{H}_f^{h,*}$, which do not need to match any of the values of the tangential fields on any side of ∂V_k but will depend on them.

$$\begin{aligned}
\hat{n}_f \times \vec{E}_f^{h,*} &= \hat{n}_f \times \vec{E}_f^{h,*}\left(\vec{E}_f^h, \vec{E}_f^{h,+}, \vec{H}_f^h, \vec{H}_f^{h,+}\right) \\
\hat{n}_f \times \vec{H}_f^{h,*} &= \hat{n}_f \times \vec{H}_f^{h,*}\left(\vec{H}_f^h, \vec{H}_f^{h,+}, \vec{E}_f^h, \vec{E}_f^{h,+}\right)
\end{aligned} \tag{19}$$

An interesting feature of DG methods is that we have several possibilities for choosing the numerical flux as long as they satisfy the following conditions [69]:

- Consistency: $\vec{E}_f^{h,*}(\vec{E}_f^h, \vec{E}_f^h, \vec{H}_f^h, \vec{H}_f^h) = \vec{E}_f^h$
- Continuity: $\vec{E}_f^{h,*}$ is at least Lipschitz continuous.
- Monotonicity: $E_f^{h,*}$ is a non-decreasing function of E_f^h and H_f^h and a non-increasing function of $E_f^{h,+}$ and $H_f^{h,+}$.

The properties of the scheme will greatly depend on the choice of the flux [59]. We will focus on the three most common

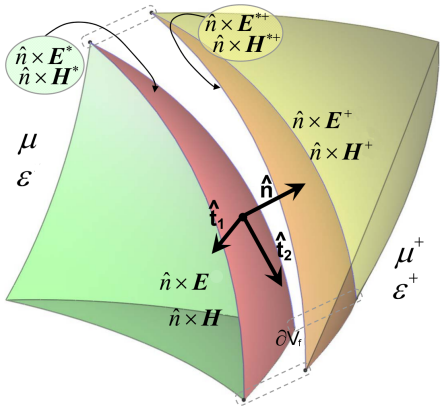

Fig. 1: Notation used for the definition of the numerical fluxes.

TABLE II: Parameters in Eq.(20) to yield centered, upwind, and partially penalized numerical fluxes. With Y and Z standing for the element admittance and impedance, respectively.

Numerical flux	Centered	Upwind	Penalized
κ_E	1/2	$\frac{Y^+}{Y+Y^+}$	$\frac{Y^+}{Y+Y^+}$
κ_H	1/2	$\frac{Z^+}{Z+Z^+}$	$\frac{Z^+}{Z+Z^+}$
ν_H	0	$\frac{1}{Y+Y^+}$	$\frac{\tau}{Y+Y^+}$
ν_E	0	$\frac{1}{Z+Z^+}$	$\frac{\tau}{Z+Z^+}$
Dispersion conv. (1-D)	h^{2p+1} (p odd)	h^{2p+3}	h^{2p+3}
Dissipation conv. (1-D)	-	h^{2p+2}	h^{2p+3}
Dispersion conv. (3-D)	h^{2p+2}	h^{2p+2}	h^{2p+2}
Dissipation conv. (3-D)	-	h^{2p+1}	h^{2p+1}
Spurious modes	Present	Attenuated	Attenuated

choices: the centered flux, the upwind flux, and the partially penalized flux. A general form for all of them is

$$\begin{aligned}
&\hat{n}_f \times \vec{E}_f^{h,*} = \\
&= \hat{n}_f \times \left(\vec{E}_f^h + \kappa_E [[\vec{E}^h]]_f + \nu_H \ \hat{n}_f \times [[\vec{H}^h]]_f \right) \\
&\hat{n}_f \times \vec{H}_f^{h,*} = \\
&= \hat{n}_f \times \left(\vec{H}_f^h + \kappa_H [[\vec{H}^h]]_f - \nu_E \ \hat{n}_f \times [[\vec{E}^h]]_f \right)
\end{aligned} \tag{20}$$

with

$$\begin{aligned}
[[\vec{E}^h]]_f &= \vec{E}_f^{h,+} - \vec{E}_f^h \\
[[\vec{H}^h]]_f &= \vec{H}_f^{h,+} - \vec{H}_f^h
\end{aligned} \tag{21}$$

Table II shows the expressions for the κ and ν factors for centered, upwind, and partially-penalized numerical fluxes. The terms which are multiplied by ν factors are known as penalization or upwind terms, and come from the solution of the Riemann problem [70]. In the case of partially-penalized fluxes, those are multiplied by the τ parameter. These terms introduce some dissipation to the scheme [71]–[73], but are essential to avoid the propagation of non-physical or spurious modes in the computational domain [10], [59] as will be shown in Section IV-E, where dissipation rates are numerically evaluated in the eigenvalue problem. When $\nu = 0$ (centered flux), there is no dissipation for either physical or spurious modes, at the cost of introducing spectral pollution to the method. In between the upwind and centered fluxes, a family of partially penalized fluxes can be defined [74], through the addition to the centered flux of dissipation terms that can be tuned to attenuate the spurious modes, and also to improve the accuracy. Other fluxes are described in detail in [59], such as the Stabilized Upwind flux. Although these fluxes have interesting properties, they require the introduction of a new DOF that would need to be evolved in time; and therefore, increase the computational cost. For this reason, it is not common to find them in the DGTD application-oriented literature.

C. Semi-discretized form

The introduction of (20) in Eq. (18), together with (14) and (15) let us write (12) and (13) in the final DG semi-discretized form

$$\begin{aligned}
\mu\mathcal{M}\frac{\partial \mathbf{H}}{\partial t} &= -\mathcal{S}\mathbf{E} \\
&- \sum_{f=1}^{N_f} \kappa_E \int_{\partial V_{(f,k)}} \vec{\boldsymbol{\psi}} \cdot \left(\hat{n}_f \times [[\vec{E}^h]]_f \right) d(\partial V) \\
&- \sum_{f=1}^{N_f} \nu_H \int_{\partial V_{(f,k)}} \vec{\boldsymbol{\psi}} \cdot \left(\hat{n}_f \times \hat{n}_f \times [[\vec{H}^h]]_f \right) d(\partial V) \\
\varepsilon\mathcal{M}\frac{\partial \mathbf{E}}{\partial t} &= \ \ \mathcal{S}\mathbf{H} \\
&+ \sum_{f=1}^{N_f} \kappa_H \int_{\partial V_{(f,k)}} \vec{\boldsymbol{\psi}} \cdot \left(\hat{n}_f \times [[\vec{H}^h]]_f \right) d(\partial V) \\
&- \sum_{f=1}^{N_f} \nu_E \int_{\partial V_{(f,k)}} \vec{\boldsymbol{\psi}} \cdot \left(\hat{n}_f \times \hat{n}_f \times [[\vec{E}^h]]_f \right) d(\partial V)
\end{aligned} \tag{22}$$

where we have followed a similar procedure for (13). On section IV-F2 we will present some particular cases of these expressions, depending on the choice of the basis.

D. Boundary conditions

The flux conditions which serve to connect adjacent elements, also serve to directly implement basic boundary conditions in a weak form, by simply modifying the jumps in (21).

1) Perfectly Electric Conducting (PEC): The PEC condition requires the tangential component of the electric field to be null and the tangential magnetic field component to be continuous, thus

$$\begin{aligned}
\hat{n}_f \times [[\vec{E}^h]]_{\text{PEC}} &= -2 \ \hat{n}_f \times \vec{E}^h \\
\hat{n}_f \times [[\vec{H}^h]]_{\text{PEC}} &= 0
\end{aligned} \tag{23}$$

2) Perfectly Magnetic Conducting (PMC): The PMC condition is the reciprocal of the PEC one,

$$\begin{aligned}
\hat{n}_f \times [[\vec{E}^h]]_{\text{PMC}} &= 0 \\
\hat{n}_f \times [[\vec{H}^h]]_{\text{PMC}} &= -2 \ \hat{n}_f \times \vec{H}^h
\end{aligned} \tag{24}$$

3) Silver-Mueller Absorbing (SMA): The first-order SMA boundary condition [38], [75] is based on considering that the fields outside the computational domain propagate as plane waves normal to the interface, $\hat{n}\times\vec{E} = Z\vec{H}$ or $\hat{n}\times\vec{H} = -Y\vec{E}$. To apply this condition to (20) is equivalent to modifying the jump terms to

$$\begin{aligned}\hat{n}_f \times [[\vec{E}^h]]_{\text{SMA}} &= -\hat{n}_f \times \vec{E}^h \\ \hat{n}_f \times [[\vec{H}^h]]_{\text{SMA}} &= -\hat{n}_f \times \vec{H}^h\end{aligned} \tag{25}$$

and using the following constants in (20)

$$\begin{aligned}\kappa_{E,\text{SMA}} &= \frac{1}{2} \\ \kappa_{H,\text{SMA}} &= \frac{1}{2} \\ \nu_{H,\text{SMA}} &= \frac{1}{2Y} \\ \nu_{E,\text{SMA}} &= \frac{1}{2Z}\end{aligned} \tag{26}$$

The SMA boundary condition provides an ideally null reflection coefficient for normal incidence. In practice, its performance is reduced by the numerical accuracy of the method with its absorbing characteristics rapidly degrading with the angle of incidence with respect to surface normal [76]. For this reason, it is is usually preferred to use Perfectly Matched Layers (PML) to truncate the computational domain. This will be described in section VII-A.

E. Convergence and spurious modes

Defining a state vector $\mathbf{q} = [\mathbf{E}\ \mathbf{H}]^T$ containing all DOF within element k, we can rewrite equations in (22) as a single equation that governs the time evolution of the system

$$\partial_t \mathbf{q}(t) = - (\mathcal{M}^q)^{-1} \left(\mathcal{S}^q \mathbf{q}(t) - \sum_{f=1}^{N_f} \mathcal{F}_f^q \left(\bar{\mathcal{E}}_f \mathbf{q}(t) - \bar{\mathcal{E}}_f^+ \mathbf{q}_f^+(t) \right) \right) \tag{27}$$

where $\mathcal{S}^q$ groups the stiffness operators, and $\mathcal{F}_f^q$ groups the flux operators acting over face f. The operator $\bar{\mathcal{E}}_f$ has the function of reordering the terms in $\mathbf{q}$ to reproduce the algebraic system (22). We have also assumed that we use a system of units in which $\varepsilon = \mu = 1$ to simplify the discussion. To further simplify this analysis, we will change the basis of the vector space in equation (27) by using an invertible operator $\mathcal{P}$ in (27) that diagonalizes the locally applied operators

$$\mathcal{W} = -\mathcal{P}^{-1}(\mathcal{M}^q)^{-1} \left(\mathcal{S}^q - \sum_{f=1}^{N_f} \mathcal{F}_f^q \bar{\mathcal{E}}_f \right) \mathcal{P} \tag{28}$$

We can also define the eigenmodes as

$$\mathbf{p} = \mathcal{P}^{-1}\mathbf{q} \tag{29}$$

and the external operators as

$$\mathcal{V}_f = -\mathcal{P}^{-1}(\mathcal{M}^q)^{-1}\mathcal{F}_f^q \bar{\mathcal{E}}_f^+ \mathcal{P} \tag{30}$$

This change of basis lets write equation (27) in the following compact form

$$\partial_t \mathbf{p}(t) = \mathcal{W}\mathbf{p}(t) + \sum_{f=1}^{N_f} \mathcal{V}_f \mathbf{p}_f^+(t) \tag{31}$$

Eq. (31) shows that the system can be stated as a system of $2N$ independent first-order ODEs with eigenfrequencies given by the eigenvalues of $\mathcal{W}$. This system contains contributions coming from the fluxes through the $\mathcal{V}_f\mathbf{p}_f^+$ terms. This result is particularly useful in studying the convergence, stability and other spectral properties of the scheme. Moreover, as it will be discussed in section V, the spectral properties of the scheme will have an important role on the maximum time step required for stability.

1) Convergence: The dispersion and dissipation of this method can be studied by comparing the computed and analytical plane-wave solutions within a computational domain with periodic boundary conditions [12], [19], [24], [72], [77]. Therefore, for an initial solution $\mathbf{q}$ with wavenumber k we obtain eigenmodes, $\mathbf{p}_j$ as the projection of the initial solution on the diagonalized space. Each of these modes has a numerical frequency $\omega_j(k) \in \mathbb{C}$ corresponding to the eigenvalues of $\mathcal{W}$. The imaginary part $\Im[\omega_j]$ corresponds to the oscillating frequency and the real part $\Re[\omega_j]$ corresponds to the numerical dissipation or amplification of eigenmode $\mathbf{p}_j$, if any. A necessary condition for convergency is $\Re[\omega_j] \leq 0$, which is always fulfilled by Galerkin methods. The numerical phase-velocities supported by the scheme are $c_j(k) = \omega_j/k$. Among them, we will label as $c_{(\text{fs})}$ the one with the phase-velocity closest to the analytical one. Therefore, we have,

$$\lim_{k\to 0} c_{(\text{fs})}(k) = \frac{1}{\sqrt{\varepsilon\mu}} \tag{32}$$

or equivalently, that the numerical solution tends to the analytical one for higher resolutions. As mentioned earlier, the numerical flux will impact the dispersion and dissipation of the numerical scheme. Table II summarizes the expected dispersive and dissipative convergences for the different numerical fluxes [14], [72].

2) Spurious modes: The solution provided by a discrete approximation must also be spectrally correct. That is, we may obtain a low error when the exactness of the solution is measured with global parameters in TD, but observe a polluted spectrum exhibiting non-physical resonances or spurious modes in FD. Therefore, we will require certain features from the numerical spectrum [24], [78] such as:

- Non pollution and completeness of the spectrum of eigenvalues and eigenvectors for a suitable resolution.
- Isolation of the discrete kernel modes.

A well-known drawback of nodal FEM is the presence of spurious modes [79]. For instance, in [24] it is shown that a grid sufficiently far from being quasi-structured together with a centered flux will make spurious modes arise at relatively low frequencies. These are commonly attributed to a variety of reasons, including an inexact representation of the underlying

de Rham complex[1].

An added advantage of DGTD over FEMTD resides in its discontinuous nature that permits spurious solutions to be removed if we use upwind or penalized fluxes [71], [72], [86], [87]. These fluxes are characterized by the addition of dissipative terms to Maxwell's equations, and are proven to attenuate spurious modes more strongly than physical modes. The effect in the spectrum of the eigenvalues in the use of different fluxes can be appreciated in Fig. 3. The use of centered fluxes results in all eigenvalues lying on the imaginary axis whether if they are physical or not. Fig. 2 shows how this issue translates into the spectrum of resonances of a PEC cavity, making the identification of physical resonances difficult.

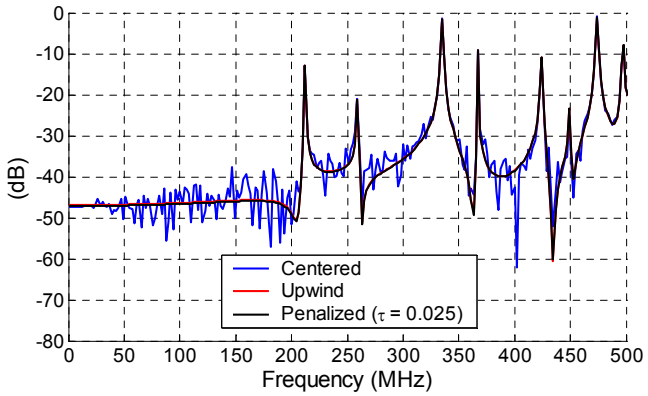

Fig. 2: Power spectrum of the electric field at an arbitrary point inside a 1 m PEC cavity. The effect of the non-attenuation of the centered flux spectrum can be appreciated compared with the upwind and penalized fluxes.

F. Vector/Nodal basis functions

Let us discuss two families of basis functions here, the vector and the nodal basis.

1) Vector basis functions: Many authors use vector basis for the implementation of DG schemes [12], [64], [88]–[90]. Vector-curl conforming basis [91]–[94] were first proposed to solve spurious-mode problems appearing in solutions using scalar basis in FEM [81]. However, these conclusions cannot be straightforwardly extrapolated to the DG case and, as has been discussed in section IV-C, the spurious-modes issue has been solved using penalized fluxes.

We can define flux matrices based on vector basis functions (22) as

$$\begin{aligned}\mu\mathcal{M}\frac{\partial \mathbf{H}}{\partial t} &= -\mathcal{S}\mathbf{E} - \kappa_E\left(\mathcal{F}_\kappa^+\mathbf{E}^+ - \mathcal{F}_\kappa\mathbf{E}\right) - \nu_H\left(\mathcal{F}_\nu^+\mathbf{H}^+ - \mathcal{F}_\nu\mathbf{H}\right)\\ \varepsilon\mathcal{M}\frac{\partial \mathbf{E}}{\partial t} &= \quad \mathcal{S}\mathbf{H} + \kappa_H\left(\mathcal{F}_\kappa^+\mathbf{H}^+ - \mathcal{F}_\kappa\mathbf{H}\right) - \nu_E\left(\mathcal{F}_\nu^+\mathbf{E}^+ - \mathcal{F}_\nu\mathbf{E}\right)\end{aligned} \tag{33}$$

[1]One way of removing this source of spurious modes is to resort to vector-based formulations [80]–[82]. Comparing vector and nodal FEM is out of the scope of this work; advantages and disadvantages of both have been reported in literature [83], [84] and would deserve a full work to be further analyzed. Another approach to mitigate spurious modes is by introducing penalty terms associated with the divergence of $\mathbf{E}$ [59], [85], at the cost of adding extra terms, and DOFs, that are to be evolved at each timestep [59].

where

$$[\mathcal{F}_\kappa]_{ij} = \int_{\partial V_{(f,k)}} \vec{\psi}_i(\vec{r}) \cdot \left(\hat{n}_f \times \vec{\psi}_j(\vec{r})\right) d(\partial V) \tag{34}$$

$$[\mathcal{F}_\kappa^+]_{ij} = \int_{\partial V_{(f,k)}} \vec{\psi}_i(\vec{r}) \cdot \left(\hat{n}_f \times \vec{\psi}_j^+(\vec{r})\right) d(\partial V) \tag{35}$$

$$[\mathcal{F}_\nu]_{ij} = \int_{\partial V_{(f,k)}} \vec{\psi}_i(\vec{r}) \cdot \left(\hat{n}_f \times \hat{n}_f \times \vec{\psi}_j(\vec{r})\right) d(\partial V) \tag{36}$$

$$[\mathcal{F}_\nu^+]_{ij} = \int_{\partial V_{(f,k)}} \vec{\psi}_i(\vec{r}) \cdot \left(\hat{n}_f \times \hat{n}_f \times \vec{\psi}_j^+(\vec{r})\right) d(\partial V) \tag{37}$$

From an implementation point of view, the main advantage of the curl-conforming vector basis functions is that $\mathcal{S}$, $\mathcal{F}_\kappa$ and $\mathcal{F}_\kappa^+$ can be shared by all the elements in a problem, since they do not depend on the geometry of the cells (size, aspect ratio and curvature) [12]. However, the mass matrices are full, with a size of $N \times N$.

2) Nodal basis functions: With nodal basis functions some simplifications are possible. The set of nodal basis functions, $\mathcal{B}_\mathrm{n}$, can be seen as a particular case of (4) in which

$$\mathcal{B}_\mathrm{n} = \left\{l_1\hat{x}, \ldots, l_{N_p}\hat{x},\ l_1\hat{y}, \ldots, l_{N_p}\hat{y},\ l_1\hat{z}, \ldots, l_{N_p}\hat{z}\right\} \tag{38}$$

with $N = 3N_p$, and N_p as the number of different scalar functions, l_i that can be obtained from a simplex element formulation [79]. We may be tempted to put the nodes $\vec{r}_n$ equidistantly for the sake of simplicity. However, as discussed in [24] and [95], the Lagrange basis with nodes located at the Legendre-Gauss-Lobatto (LGL) quadrature points is a better choice, obtaining low condition numbers for the local matrices even at high p orders.

Using the nodal basis (38), we have that

$$\begin{aligned}\vec{E}^h &= \sum_{j=1}^{N} E_j^h \vec{\psi}_j\\ &= \sum_{j=1}^{N_p} E_j^h l_j \hat{x} + \sum_{j=N_p+1}^{2N_p} E_j^h l_j \hat{y} + \sum_{j=2N_p+1}^{3N_p} E_j^h l_j \hat{z}\\ &= \sum_{j=1}^{N_p} \vec{E}_j^h l_j \doteq \vec{\mathbf{E}}^T \boldsymbol{l}\end{aligned} \tag{39}$$

and similarly, for $\vec{H}^h \doteq \vec{\mathbf{H}}^T \boldsymbol{l}$. When expressed using the nodal basis (38), the operators $\mathcal{M}$ and $\mathcal{S}$ are composed of blocks that decouple some Cartesian components of the vectors [83],

$$\mathcal{M} = \begin{pmatrix} \mathcal{M}_n & & \\ & \mathcal{M}_n & \\ & & \mathcal{M}_n \end{pmatrix} \tag{40}$$

$$\mathcal{S} = \begin{pmatrix} & -\mathcal{S}_n^z & \mathcal{S}_n^y \\ \mathcal{S}_n^z & & -\mathcal{S}_n^z \\ -\mathcal{S}_n^y & \mathcal{S}_n^x & \end{pmatrix} \tag{41}$$

Where $\mathcal{M}_n$ and $\mathcal{S}_n^{x,y,z}$ have size $N_p \times N_p$. The flux terms are also simplified, as they will now need only to account for fields in nodes at face f. When a nodal basis is used, the equation (22) can be expressed for non-curved elements, as

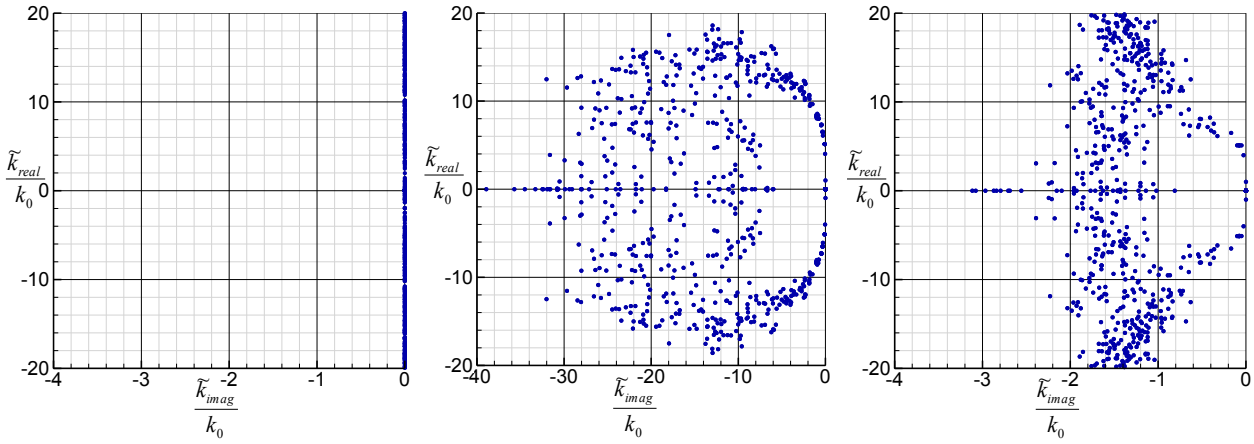

(a) Centered flux ($\tau = 0.0$)

(b) Upwind flux ($\tau = 1.0$)

(c) Penalized flux ($\tau = 0.1$)

Fig. 3: Normalized spectrum of the DG operator for a cubic domain (meshed with 24 tetrahedrons) with periodic boundary conditions. We can see how the centered flux does not provide an isolated kernel, contrary to the upwind and penalized fluxes.

TABLE III: Comparison of vector and nodal basis

	Vector		Scalar[a]	
	Linear	Curved	Linear	Curved
$\mathcal{M}$ size	$N \times N$		$N_p \times N_p$	
$\mathcal{S}$ size	$N \times N$		$3(N_p \times N_p)$	
$\mathcal{F}$ size	4 sparse matrices		$N_p \times (N_f N_{fp})$	$N_p \times (N_f N_{fp})^b$
Shared operators[c]	$\mathcal{S}$, $\mathcal{F}_\kappa$, $\mathcal{F}_\kappa^+$		$\mathcal{M}$, $\mathcal{F}$	None

[a]The number of nodes for scalar basis is $N_p = N/3$. The number of face nodes N_{fp} is $(p+1)(p+2)/2$! for tetrahedrons and $(p+1)^2$ for hexahedrons.
[b]For curved cells, the storage and number of operations needed are significantly higher, varying depending on the implementation.
[c]Without considering identical cells in which all operators can be shared. Neglecting scaling factors.

$$
\begin{aligned}
&\mu\mathcal{M}\frac{\partial\vec{\mathbf{H}}}{\partial t} = \\
&= -\mathcal{S}\vec{\mathbf{E}} - \sum_{f=1}^{N_f}\mathcal{F}_f\left[\hat{n}_f \times (\kappa_E[[\vec{\mathbf{E}}]]_f + \nu_H\hat{n}_f \times [[\vec{\mathbf{H}}]]_f)\right] \\
&\varepsilon\mathcal{M}\frac{\partial\vec{\mathbf{E}}}{\partial t} = \\
&= \mathcal{S}\vec{\mathbf{H}} + \sum_{f=1}^{N_f}\mathcal{F}_f\left[\hat{n}_f \times \left(\kappa_H[[\vec{\mathbf{H}}]]_f - \nu_E\ \hat{n}_f \times [[\vec{\mathbf{E}}]]_f\right)\right]
\end{aligned}
\tag{42}
$$

with

$$
\mathcal{F}_f = \begin{bmatrix} \mathcal{F}_n^f & & \\ & \mathcal{F}_n^f & \\ & & \mathcal{F}_n^f \end{bmatrix} \tag{43}
$$

where

$$
[\mathcal{F}_n^f]_{ij} = \begin{cases} \int_{\partial V_{(f,k)}} l_i(\vec{r}) l_j(\vec{r}) d(\partial V) & \text{if } \vec{r}_{n,i} \in \partial V_{(f,k)} \\ 0 & \text{if } \vec{r}_{n,i} \notin \partial V_{(f,k)} \end{cases} \tag{44}
$$

has a size of $N_p \times N_{fp}$ with N_{fp} being the number of nodes at face f. This implies that nodal basis scale computationally better than vector basis when we increase the order of basis functions p; being this the main reason why nodal basis is usually preferred for high order schemes [24]. $\mathcal{F}_n$ and $\mathcal{M}_n$ are the same for all elements except for a scaling factor; therefore we do not need to store them more than once for the entire simulation. Note that to to obtain the equations (42) we assume that $\hat{n}_f$ is constant for the flux integral terms in (22); therefore this simplification in the flux integral is not valid if we work with curved elements (see Section IV-G).

G. Curved cells

One of the most appealing features of DG methods is that they can be formulated for higher-order geometric elements which offer a better geometrical adaptivity [24], [96]–[99]. Most available open-source [100] and commercial meshers [101] offer the possibility of meshing with quadratic elements and techniques-exist allowing higher orders [102]. Using quadratic elements allows us to use fewer of them to accurately discretize a curved surface, thus implying that their size can be larger.

The implementation of this technique requires the usage of quadrature integrals [103] because the complexity of the involved Jacobians needed to transform the reference element into the actual mesh element which results in integrals that cannot be solved analytically. For nodal basis, this technique needs to store information of the operators needed by the curved element, thus requires storing one flux matrix (44) per cubature point [24] or alternatively, one operator per each term in (20) containing a normal unit vector. These requirements introduce a significant computational overhead

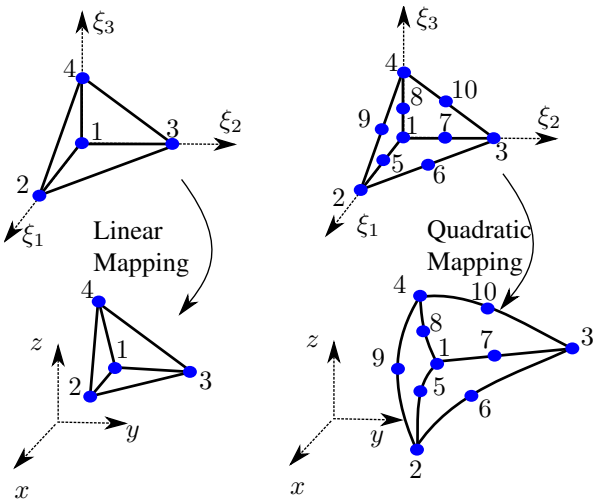

Fig. 4: Mapping from the reference element for linear (first geometrical order) and quadratic (second geometrical order) tetrahedrons.

both in memory, as well as a number of operatins that can be a factor, depending on the application.

To illustrate the possibilities of this approach, Fig. 5 shows a comparison of the results obtained with meshes using the same number of quadratic and linear elements. It can be appreciated that the improved geometry adaptivity provides a better result for the same number of elements.

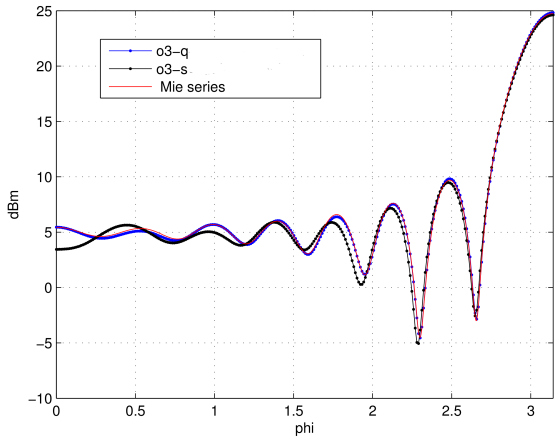

Fig. 5: RCS at 450 MHz of a 1m radius PEC sphere meshed with the same number of linear and quadratic tetrahedrons and a spatial basis of order $p = 3$. Results obtained with GEGUGR SEMBA software (www.ugrfdtd.es).

H. Non-conformal and hybrid meshes

Another advantage of using numerical fluxes to exchange information between elements is the possibility of using non-conformal interfaces between elements [104]–[107]. This is to connect elements that do not share a whole face but a portion of it. This feature is interesting because there are applications with very intricate geometries where a conformal mesh may be very difficult to obtain, or domains that require different element sizes. In DG, thanks to the flux functions, the interface between non-conformal meshes can be posed in a natural way. In [104], [106], [107] the authors find that the convergence of the method remains the same as with conformal meshes.

The use of non-conformal meshes allows us to interface tetrahedrons with hexahedrons in the transition regions, as demonstrated in [106], [107]; and therefore, use hybrid meshes that combine several kinds of elements. Another possibility for the transition region is to use pyramidal elements. This approach has been studied in [108], [109]. In the case of non-conformal meshes, this can be done in a natural way by making use of the flux terms. The advantage of using hybrid meshes is that we can have the best of two worlds [4], [64], [88], e.g. tetrahedrons can adapt better to surfaces in complicated geometries, or hexahedrons for the discretization of zones where structured mesh could be used, enabling larger time steps and a reduced number of degrees of freedom.

V. Time integration

In this section, we present two time integration methods that are also the most popular choices, in conjunction with the DG semidiscretizations presented in the previous section. Table IV presents a summary of features of different time integration methods.

A. Leapfrog time integration

1) Second order leapfrog (LF2): The second-order leapfrog method [120] is applied by alternately evolving the $\mathbf{E}^n$ and $\mathbf{H}^{n+1/2}$ fields, arbitrarily defined at times t_n and $t_n + \Delta t/2$ respectively. This implies that we do not have a fully defined state vector in the sense of eq. (27) for a given time t. To obtain the future values from a present state, the following algorithm is applied

$$\begin{aligned}\mathbf{E}^{n+1} &= \mathbf{E}^n + \Delta t\ \mathcal{L}_E^h\left(\mathbf{H}^{n+1/2}, \mathbf{E}^n\right)\\ \mathbf{H}^{n+3/2} &= \mathbf{H}^{n+1/2} + \Delta t\ \mathcal{L}_H^h\left(\mathbf{E}^{n+1}, \mathbf{H}^{n+1/2}\right)\end{aligned} \tag{45}$$

with $\mathcal{L}_E^h$ and $\mathcal{L}_H^h$ being the equations (22), respectively. When centered fluxes are used, the $\mathcal{L}_E^h$ and $\mathcal{L}_H^h$ operators use only $\mathbf{H}^{n+1/2}$ and $\mathbf{E}^{n+1}$ as arguments, respectively. This implies that the scheme is reversible in time and will preserve energy as long as the timestep used is below a maximum value h_t set by a CFL-like condition [90], [118], [120]. The use of upwind or penalized fluxes would imply the need of averaging between the next and previous semi-integer time steps in the dissipation terms, thus resulting on a globally implicit scheme. To avoid this we need to use a backwards approximation [12], [61] and use the last previous known value instead of averaging.

2) Convergence and spectral properties of the LF2 scheme: The study of the full spectrum of $\mathcal{W}$ obtained in (28) is also useful as its properties impose limitations in regards to the time-integration. The LF2 method has the following stability requirement on its timestep h_t [12], [74], [121]

$$h_t \leq 1/\Im[\omega_{k,j}] \tag{46}$$

and therefore is constrained by the largest imaginary part among all eigenvalues of (28). Equation (46) needs to solve

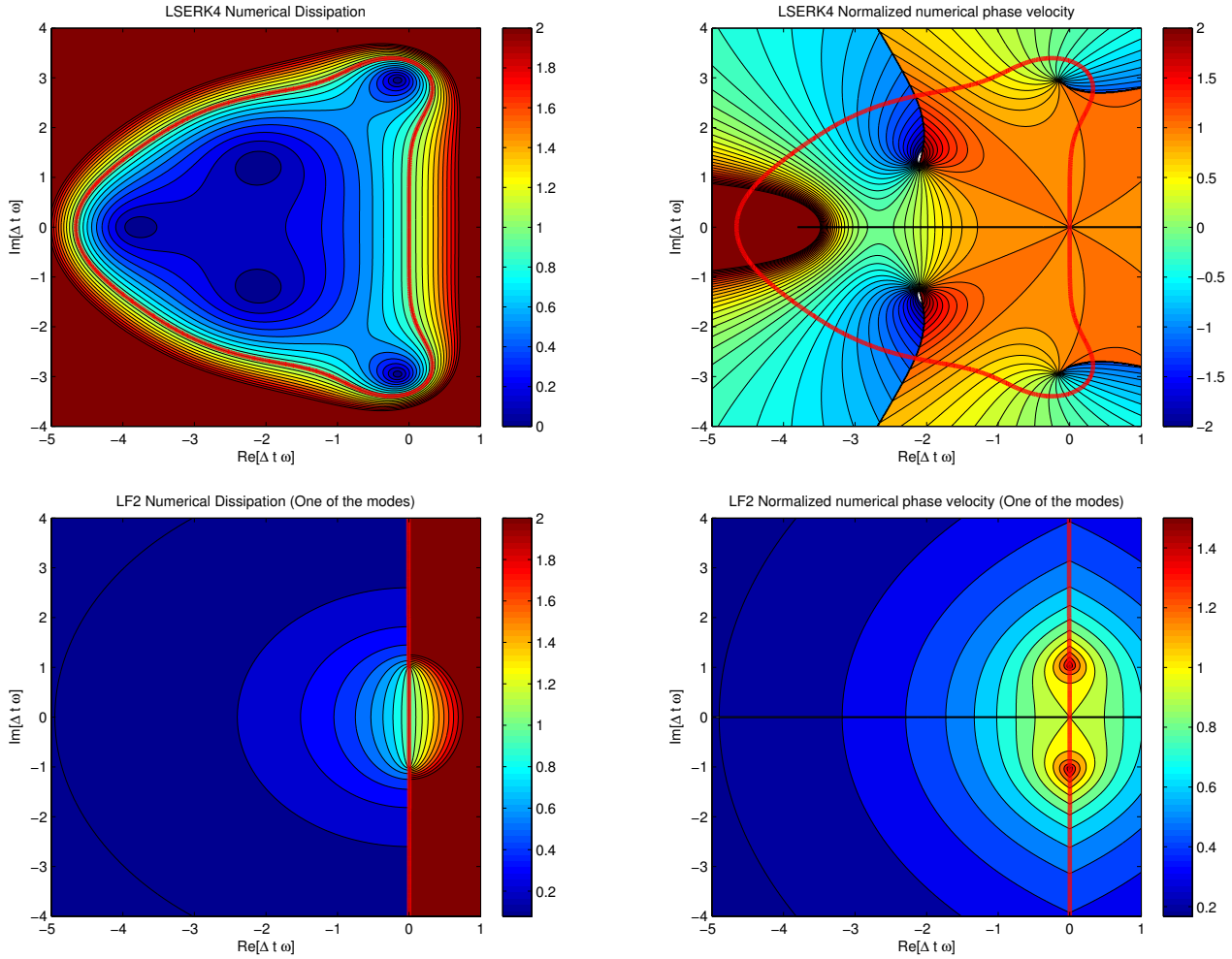

Fig. 6: Dissipation factors (left) and normalized phase velocities (right) for the LSERK4 (up) and LF2 (down) schemes. All the semi-discrete eigenvalues calculated depicted in Fig. 3 must lie within the regions delimited by the thick red line to ensure the stability of the fully discrete scheme. LF2 supports two modes arising from two solutions for the growing factor. Only the positive one is represented. Please note that the final form of the dissipation and phase velocities depend on the combination of the two modes [110].)

a complex eigenvalue problem for each specific problem. To avoid this, we can use heuristic or analytical closed conditions [74], [87], [122]. For instance, for $p = 1$ with centered flux we have that

$$h_t \lesssim \frac{12}{8+\sqrt{40}} \frac{V_k}{c_k \partial V_k} \tag{47}$$

Therefore, the LF2 algorithm has a semi-infinite stability region which may not be bounded with respect to a value of the real axis, depending on how the method is initialized [110]. This relieves this method from some bounds in material properties, and additional algebraic constraints that are present for methods with closed-stability regions [123].

3) Higher-order LF: A N-th order leapfrog (LFN) time integrator applied to DG is discussed in [104]. These techniques can obtain high-order convergence in time avoiding the use of larger stencils. Thus, these methods allow us to retain the high-order convergence in the fully discretized numerical scheme. They also allow larger time steps than for LF2, while retaining their symplectic non-dissipative nature. However, they require $N/2$ times more memory storage and $N-1$ times more arithmetic operations per time step than LF2. This is the main reason why their usage is not widespread when higher-order convergences are demanded, where the LSERK is the most typical approach.

B. Low Storage Explicit Runge Kutta time integration

1) The LSERK4 scheme: The low-storage five-stage fourth-order Explicit Runge-Kutta method (LSERK4) [24], [111], [124] allows us to achieve a fourth-order convergence in the time integration, storing only one additional unknown per degree of freedom. For a given vector representing the state of an element k, i.e. $\mathbf{p}_k(t) = \mathbf{p}_k^n$ we can find an approximate solution state $\mathbf{p}_k(t+\Delta t) = \mathbf{p}_k^{n+1}$ applying the following

TABLE IV: Comparison of different time integration methods

	LF2	LSERK4	*Tailored* LSERK(m,n)[a]	SSP-RK(m)[b]	STDG
Order of convergence	h_t^2	h_t^4	h_t^n	h_t^m	$h_t^{2p_t+1}$
Explicit form	Yes	Yes	Yes	Yes	Pseudo
Dissipative	No	Yes	Yes	Yes	Yes/No[c]
Stages stored	1[d] or 1.5[e]	2	2	m	2 or p_t+1
Stability region	Semi-infinite	Closed	Closed[f]	Closed[g]	Semi-infinite
LTS	Yes [20], [74]	Yes [20], [116]	Not demonstrated	Not demonstrated	Pseudo [117]
IMEX	Usually CN2 [62], [118]	Implicit RK [119]	Not demonstrated	Not demonstrated	Pseudo

[a]LSERK with m stages and order n; as described in [111], [112].
[b]With m stages; as described in [71], [113].
[c]Non dissipative implementations [114], [115].
[d]With centered fluxes.
[e]With upwind fluxes.
[f]And customized to fit the eigenvalues of the DG operators [111], [112], therefore allowing larger h_t than LSERK4.
[g]Larger than with LSERK4, allowing larger h_t.

algorithm, using the notation introduced in (31)

$$\begin{aligned}\mathbf{p}^{(0)} &= \mathbf{p}^n,\\ \mathbf{r}^{(i)} &= a_i\mathbf{r}^{(i-1)} + \Delta t\left(\mathcal{W}\mathbf{p}^{(i-1)} + \sum_f \mathcal{V}_f\mathbf{p}_f^{(i-1),+}\right),\\ \mathbf{p}^{(i)} &= \mathbf{p}^{(i-1)} + b_i\mathbf{r}^{(i)},\\ \mathbf{p}^{(n+1)} &= \mathbf{p}^{(5)}\end{aligned} \tag{48}$$

with $i \in [1,...,5]$ and the coefficients a_i, b_i and c_i taking the values indicated in Table V and $\mathbf{r}$ being the residue. The LSERK4 scheme is one of the most used methods in high–order Discontinuous Galerkin semi–discretizations because of its low dispersion and dissipation errors. Contrary to other RK implementations, the low–storage version requires the storage of only twice the number of degrees of freedom in the scheme at the expense of one additional stage. Despite its many advantages, LSERK4 has a higher computational cost than LF2, and the numerical dissipation it introduces can be a factor depending on the application. For this reason, a number of authors have proposed alternatives for the classical LSERK4 scheme [71], [111], [112].

TABLE V: Coefficients for the low-storage five-stage fourth-order Explicit Runge–Kutta method (LSERK4)

s	a_s	b_s	c_s
1	0	$\frac{1432997174477}{9575080441755}$	0
2	$-\frac{567301805773}{1357537059087}$	$\frac{5161836677717}{13612068292357}$	$\frac{13612068292357}{9575080441755}$
3	$-\frac{2404267990393}{2016746695238}$	$\frac{1720146321549}{2090206949498}$	$\frac{22526269341429}{6820363962896}$
4	$-\frac{-3550918686646}{2091501179385}$	$\frac{3134564353537}{4481467310338}$	$\frac{2006345519317}{3224310063776}$
5	$-\frac{1275806237668}{842570457699}$	$\frac{2277821191437}{14882151754819}$	$\frac{28032321613138}{2924317926251}$

2) Convergence and spectral properties: RK methods are constrained by the spectra of the operator $\mathcal{W}_k$; i.e. all the eigenvalues of $\mathcal{W}_k$ must lie inside the stability region of the RK scheme (Fig. 6). The LSERK4 method allows for slightly larger time steps than LF2 but imposes constraints when dealing with dispersive materials [123]. LSERK methods comprise irregular closed loci in the complex plane [111], [125] in which the eigenvalues of (28) must lie to ensure stability. Consequently, the timestep must be chosen sufficiently small, e.g. for a nodal basis, the following inequality must hold [24]

$$\Delta h_{t,k} \leq \frac{C}{c_k}\min_i \frac{\Delta h_{ki}}{2} \tag{49}$$

where $\min_i \Delta h_{ki}$ indicates the minimum distance between nodes in element k, c_k is the maximum speed of light in the element k, and C is a constant.

C. Achieving larger global timesteps

The presence of small-sized elements imposes constraints to the maximum size of the time step, severely affecting the computational efficiency. As we can appreciate from (46) and (49), the maximum time step allowed to ensure stability is proportional to an inverse power of the size of the elements. This has been a topic of intense research aiming to overcome the global limitations imposed by a local condition. Some existing solutions are discussed below.

1) Local Time Stepping (LTS): The most straightforward approach to deal with the global timestep restrictions imposed by the presence of local small-sized elements is to devise a LTS technique by which these elements are evolved using a smaller timestep. To do so, the elements are clustered in different groups, or tiers, according to the maximum timestep allowed by the smallest element in the tier. The interfaces between elements within the same tier are treated in the usual way; however, the interfaces between tiers will require a special treatment because the smaller tiers require field values that the larger steps do not compute.

For the LF2 method, we can find at least three alternatives:

- In [74], [120] and [90], the authors use a method, initially devised by Montseny, in which the last available field coefficient is used when the smaller tiers require intermediate time-step values from larger tiers. The main advantage of this technique is that it preserves the reversibility of the scheme and in consequence, the scheme remains non-dissipative. On the other hand, it introduces some additional numerical dispersion, and a penalization of the stability condition.

- In [12] the LTS is accomplished interpolating the field unknowns in an interface region between the different tiers. This interpolation improves the accuracy and stability of the technique compared with Montseny's method.
- In [20] a technique called causal-path LTS (CPLTS) is applied. This technique consists of computing auxiliary fields in a shrinking buffer zone whenever they are needed by the smaller time-step tier. Once they have been used by the smaller tier, they are casted away and the higher tier is evolved using the original values. As shown in [20], the scheme has better dispersive properties than Montseny's and allows for a better assortment of tiers. However, it introduces some dissipation and it cannot be used with centered fluxes and requires more arithmetic operations.

For RK methods we can also find several alternatives:

- The CP-LTS technique previously discussed for LF2 can also be applied to RK schemes, as discussed in [20]. Although the dispersive properties do not seem to be significantly affected when low spatial orders are used, this technique introduces a significant amount of numerical dissipation.
- A similar concept is shown in [126]. First, the whole domain is evolved using the higher-tier timestep. Then, the values of the solution that have been polluted by the usage of a timestep larger than allowed are cast away. To compute the values in the lower-tier region an interpolation in the boundary is performed.
- In [24], [127] a scheme allowing each element to be advanced with its own individual and optimal timestep is shown. This technique, called Arbitrary High-Order Derivatives (ADER) consists of expanding the solution in Taylor series in time. These time derivatives are then replaced by space derivatives using a Cauchy-Kovalevskaya procedure. The resulting scheme is high-order accurate in space and time.

2) Implicit-Explicit (IMEX) schemes: Another technique to improve the global efficiency of the scheme is to use an implicit time integrator in the regions presenting a higher stiffness while using a usual explicit time integrator in the remaining domain. This approach aims to benefit from the unconditional stability that is usually a characteristic of implicit schemes. However, as opposed to LTS, these techniques cannot be used recursively, and a large number of unknowns of the implicit part can reduce the computational benefits for meshes with highly disparate sizes. In [119], implicit and explicit RK schemes are applied to several types of PDEs. In [62], [118], the authors show an IMEX technique applied to Maxwell's equations using a second order Crank-Nicolson (CN2) scheme for the implicit part and a LF2 scheme for the explicit one.

3) Predictor-Corrector time integration: A predictor-corrector scheme is an algorithm that proceeds in two steps. First, the prediction step calculates a rough approximation. Second, the corrector step refines the initial approximation using another means. In [128] an application of a predictor-corrector scheme is proposed and in [129] is applied to a DGTD method to solve Maxwell's equations. This lets the authors significantly increase the timesteps compared with other methods at the expense of a moderate increase in memory.

4) Tailored LSERK schemes: In [111], [112] the authors explore the usage of higher number of stages and different orders for new LSERK schemes. The approach they take is to make assumptions over the form of the spectrum based on several typical cases, and then find coefficients for the RK schemes by fitting their stability regions to that spectrum. They conclude that the increase in the size of timesteps offsets the inclusion of new stages, and therefore they are able to obtain improvements of up to a $40-50\%$.

5) Strong Stability Preserving RK (SSP-RK) schemes: In [71], [113] a Strong Stability Preserving Runge-Kutta (SSP-RK) technique is used. This scheme has a larger stability region, thus allowing us to use a larger h_t. At each time step, the method needs to evaluate m stages achieving an m order of convergence. In [71], the authors demonstrate an improvement in the number of operations needed by the scheme. The main drawback of this method is that it needs to store m stages, thus significantly increasing the memory consumption.

6) Space-time Discontinuous Galerkin (STDG): As we have seen in previous sections, the typical approaches consist on obtaining a DG spatial semi-discretization that is then evolved with an explicit time integrator algorithm. On the contrary, the STDG approach consists of applying the DG also in the time dimension [21], [114], [115], [117], [130], [131]. The resulting scheme, therefore, extends to the time dimension most of the properties of spatial DG, such as the high-order convergence. There are many ways of implementing this concept; some approaches arise to non-dissipative [114], [115] schemes, others result in pseudo-explicit methods [21], [117], [130], or allow a significant freedom in the election of the time step [21].

VI. Electromagnetic Sources

Electromagnetic sources in DGTD are almost a direct extension of the techniques already developed for FDTD [132]. For instance, those based on Huygens's principle [7], [133] employ a division of the computational domain into two zones, the Total Field Zone (TFZ) and the Scattered Field Zone (SFZ) to permit the simulation of field incidence, being the main differences between the FDTD and DGTD implementations due to the staggered nature of FDTD.

A. Plane wave

Let us consider the case of a known incident wave propagating in a specific region as the one shown in Fig. 7. The implementation of Huygen's principle on a surface where the field values are $\vec{E}^{\text{inc}}(t)$ and $\vec{H}^{\text{inc}}(t)$ yields an equivalent problem for which the fields are null outside that surface (SFZ) and propagates inside it (TFZ). This discontinuity is naturally implemented in DGTD [7], [27] through the jumps (21) used to calculate the flux across the face of an element k, which need to be modified, just in the TF region, according to

$$\begin{aligned}\hat{n}_f \times \vec{E}^{h,+}_{\text{TF}}(t) &= \hat{n}_f \times \left(\vec{E}^{h,+}(t) + \vec{E}^{h,\text{inc}}(t)\right)\\ \hat{n}_f \times \vec{H}^{h,+}_{\text{TF}}(t) &= \hat{n}_f \times \left(\vec{H}^{h,+}(t) + \vec{H}^{h,\text{inc}}(t)\right)\end{aligned} \tag{50}$$

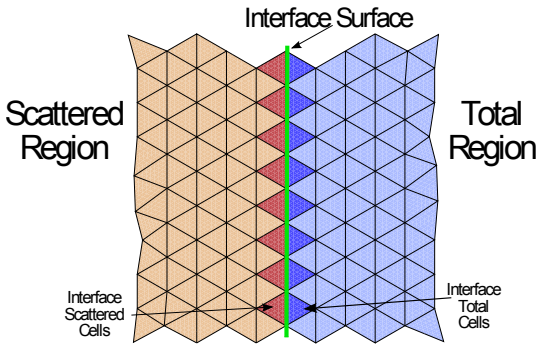

Fig. 7: Scattered field (orange) and total field regions (blue). The elements that need to have altered fluxes are marked in darker colors.

If k is in the SF region the fields calculated at the face interfacing with the TFZ are modified to

$$\hat{n}_f \times \vec{E}^{h,+}_{\text{SF}}(t) = \hat{n}_f \times \left(\vec{E}^{h,+}(t) - \vec{E}^{h,\text{inc}}(t)\right)$$
$$\hat{n}_f \times \vec{H}^{h,+}_{\text{SF}}(t) = \hat{n}_f \times \left(\vec{H}^{h,+}(t) - \vec{H}^{h,\text{inc}}(t)\right) \quad (51)$$

Note that the fields $\vec{E}^{\text{inc}}$ and $\vec{H}^{\text{inc}}$, can describe any kind of waves such as plane waves, linearly or elliptically polarized, or even spherical waves with minor modifications. In FDTD, the TFZ and SFZ are separated by one cell introducing some numerical errors. On the contrary, for DGTD, the discontinuous nature of the method allows us to use the same geometrical surface as the TFZ/SFZ interface. Moreover, the SFZ can be pushed directly onto the computational domain and be backed with an SMA-BC. On this surface we can also apply a near-to-far-field technique [134] which can also be applied to compute RCS or radiation patterns of antennas.

B. Local sources and radiation patterns

The most obvious way to model a point current source $\vec{J}_s(t, \vec{r}_0)$ is by directly modifying the magnetic field corresponding to the node in the position $\vec{r}_0$ shared by it [27], [135]. Therefore using

$$\vec{H}^{\text{inc}}(t) = \hat{n} \times \vec{J}_s(\vec{r}_0, t) \quad (52)$$

in (50) and (51). However, as pointed out in [27], [135] the Lagrange polynomials are not able to resolve the field values well in the vicinity of $\vec{r}_0$, where the fields are theoretically infinite, forcing the refining of the mesh around that point, and thus increasing drastically the computational cost. This justifies the introduction of an alternative solution, through the use of localized sources, described below. If we use a formalism similar to the defined for the TFZ/SFZ illumination, we can avoid defining the fields in the region closest to the point source [7], [135]. Therefore, for a dipole we could use the analytical expressions describing the fields $\vec{E}^{\text{inc}}(t)$ and $\vec{H}^{\text{inc}}(t)$ at the position of the interface. These expressions are evaluated using theoretical equations such as the ones that can be found in [136] for an electric dipole. The advantage of this technique is that the field at the interface can be defined freely so it is possible to use it to define antenna radiation patterns including near fields.

C. Waveports

1) TEM port: A TEM mode (e.g. for a coaxial port) can be directly injected into the port in a weak manner through the flux terms by adding $\vec{E}^{h,\text{inc}}$ and $\vec{H}^{h,\text{inc}}$ to the jump terms in (21). For the first coaxial TEM mode, these terms are

$$\vec{E}^{h,\text{inc}}(t) = V^{\text{inc}}(t)\frac{1}{\log(b/a)}\frac{1}{\rho}\hat{\rho}$$
$$\vec{H}^{h,\text{inc}}(t) = V^{\text{inc}}(t)\frac{1}{Z\log(b/a)}\frac{1}{\rho}\hat{\phi} \quad (53)$$

in (50) and (51), with a and b being the inner and outer radii of the conductors forming the coaxial and $V^{\text{inc}}(t)$ the time variation of the excitation signal. The TEM ports are accurately truncated with a SMA boundary condition (described in section IV-D3) that can be located in the same surface of the port.

2) Waveguide modes:

a) Arbitrary shape wave guides: In [50], [66], Lou *et al.* describe a method to excite arbitrarily shaped waveguides in a FEMTD scheme that can be simply extrapolated to DGTD. To do this, Lou starts by solving the 2D Helmholtz problem at the plane forming the waveport to get the eigenvectors and eigenfrequencies. Then these FD solutions are solved in TD by applying the inverse Laplace transform. This approach is also useful in truncating the waveguide in a very efficient and accurate manner. The absorption in waveguides is particularly problematic when absorbing boundary conditions (ABC) are used, because the waves are always imping over the absorbing conditions with a high angle when their frequency is close to the cut frequencies of the supported modes.

b) Rectangular waveguide: A simplified version of [50], [66] can be implemented directly by using the analytical TE and TM modes. For a rectangular waveguide, we have the following analytical expressions for the supported modes [136],

$$\vec{H}_{\text{TE}_{mn}}(\omega) = \begin{pmatrix} \frac{\gamma_{mn}}{k^2_{mn}}\frac{\pi m}{a}\sin\frac{\pi m x}{a}\cos\frac{\pi n y}{b} \\ \frac{\gamma_{mn}}{k^2_{mn}}\frac{\pi n}{b}\cos\frac{\pi m x}{a}\sin\frac{\pi n y}{b} \\ \cos\frac{\pi m x}{a}\cos\frac{\pi n y}{b} \end{pmatrix} B_{mn}(\omega) \quad (54)$$

$$\vec{E}_{\text{TE}_{mn}}(\omega) = \begin{pmatrix} \frac{\pi n}{b}\cos\frac{\pi m x}{a}\sin\frac{\pi n y}{b} \\ -\frac{\pi m}{a}\sin\frac{\pi m x}{a}\cos\frac{\pi n y}{b} \\ 0 \end{pmatrix} B_{mn}(\omega)\frac{\eta\gamma_0}{k^2_{mn}} \quad (55)$$

$$\vec{H}_{\text{TM}_{mn}}(\omega) = \begin{pmatrix} \frac{\pi n}{b}\sin\frac{\pi m x}{a}\cos\frac{\pi n y}{b} \\ -\frac{\pi m}{a}\cos\frac{\pi m x}{a}\sin\frac{\pi n y}{b} \\ 0 \end{pmatrix} A_{mn}(\omega)\frac{\eta^{-1}\gamma_0}{k^2_{mn}} \quad (56)$$

$$\vec{E}_{\text{TM}_{mn}}(\omega) = \begin{pmatrix} \frac{\gamma_{mn}}{k^2_{mn}}\frac{\pi m}{a}\cos\frac{\pi m x}{a}\sin\frac{\pi n y}{b} \\ \frac{\gamma_{mn}}{k^2_{mn}}\frac{\pi n}{b}\sin\frac{\pi m x}{a}\cos\frac{\pi n y}{b} \\ \sin\frac{\pi m x}{a}\sin\frac{\pi n y}{b} \end{pmatrix} A_{mn}(\omega) \quad (57)$$

where $\gamma_{mn}(\omega) = \sqrt{\frac{(j\omega)^2}{c^2} + k^2_{mn}}$, $k^2_{mn} = \left(\frac{m\pi}{a}\right)^2 + \left(\frac{n\pi}{b}\right)^2$, and $\eta = \sqrt{\mu/\varepsilon}$. $B_{mn}(\omega)$ and $A_{mn}(\omega)$ are the spectral components of the mode mn. In the Laplace domain, $\gamma_0 = s/c$ and $\gamma_{mn} = \sqrt{s^2/c^2 + k^2_{mn}}$, which in the time domain can be represented

with the following operators [66]:

$$\gamma_0 = \mathcal{L} = \frac{1}{c}\frac{\partial}{\partial t} \tag{58}$$

$$\gamma_{mn} = \mathcal{H}_{mn} = \frac{1}{c}\frac{\partial}{\partial t} + h_{mn}(t)* \tag{59}$$

where $*$ stands for convolution in time and the impulse response of the system $h_{mn}(t)$ is given by [137]

$$h_{mn}(t) = \frac{k_{mn}}{t} J_1(k_{mn}ct)u(t) \tag{60}$$

$u(t)$ denoting the unit step function and $J_1(\cdot)$ the Bessel function of the first kind. If we are using a Gaussian excitation for the mode $A_{mn} = f(t)$ of the form

$$f(t) = u(t)\exp\left[-\left(\frac{t-\mu}{\sigma\sqrt{2}}\right)^2\right] \tag{61}$$

we can write eq. (58) and (59), using a numerical convolution technique, as

$$\gamma_0 f(t^n) = \frac{1}{c}\left[\frac{\partial f(t)}{\partial t}\right]_{t=t_n} \tag{62}$$

$$\gamma_{mn} f(t^n) \simeq -\frac{f(t^n)}{c}\frac{2}{\sigma\sqrt{2}}\left(\frac{t^n-\mu}{\sigma\sqrt{2}}\right) + \Delta t\sum_j^n h_m(t^j) f(t^{n-j}) \tag{63}$$

that enables the computation of (54), (55), (56) and (57), in the time domain.

VII. Advanced material modeling

A. Conformal Perfectly Matched Layer

Perfectly Matched Layers (PMLs) were introduced for the first time in [138] as a way to truncate the computational domain in open-region scattering problems. They can actually be seen as a special kind of non-Maxwellian dispersive anisotropic material [33]. The main advantage of PMLs over other ABC is that they are largely independent of frequency, wave polarization, and angle of incidence. They also have extremely small reflection errors. PMLs are material-independent and can truncate domains with inhomogeneous, dispersive, and non-linear materials. There are several variants of PMLs [139]–[144], mainly developed in the FDTD context, with features particularly well-suited for different applications: e.g., in [139] the author presents an Auxiliary Differential Equation (ADE) form of a multi-pole Complex-Frequency Shifted PML that presents advantages when it is extended to high-order methods. Equivalent convolutional formulation can also be used [145].

The Conformal PML (CPMLs) allow us in DGTD to add PMLs extruding the outer surface of the computational domain [12], [144]. The only geometrical restriction to this formulation is that the PMLs must form a convex-closed region when viewed from the outside, or they will be dynamically unstable [146].

Let us consider the setup of Fig. 8 representing a right-handed reference frame called a Darboux frame at a point P of an internal surface S. This frame is defined by an orthonormal local vector-basis $\mathbf{u}_1$, $\mathbf{u}_2$ and $\mathbf{u}_3$. $\mathbf{u}_1$ and $\mathbf{u}_2$

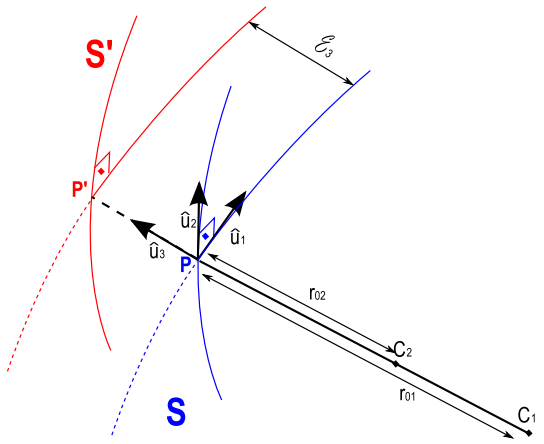

Fig. 8: Darboux frame.

which are tangent to S at a point P along the principal lines of curvature. The third component is obtained from the other two as $\mathbf{u}_3 = \mathbf{u}_1 \times \mathbf{u}_2$. We can write $\mathbf{u}_i$ in terms of local coordinates ξ_i as $\mathbf{u}_i = (\partial\vec{r}/\partial\xi_i)/|\partial\vec{r}/\partial\xi_i|, i = 1,2,3$ where $\vec{r}$ is the position vector. With these definitions $\xi_3 = 0$ represents the surface S. The unit vectors are functions of ξ_1 and ξ_2 only. Within the defined local reference frame, the radii of curvature $r_{01}(\xi_1,\xi_2)$ and $r_{02}(\xi_1,\xi_2)$ are positive (for convex S) and we also have that at a point P' the radius r_j can be expressed as $r_j(\xi) = r_{0j}(\xi_1,\xi_2) + \xi_3$.

We will also use the the Lamé coefficients, h_i which in the Darboux frame are

$$h_1 = r_1/r_{01} \tag{64}$$

$$h_2 = r_2/r_{02} \tag{65}$$

$$h_3 = 1 \tag{66}$$

The conformal PML[2] can be obtained through a complex stretching on the normal coordinate ξ_3:

$$\begin{aligned}\xi_3 \to \tilde{\xi}_3 &= \int_0^{\xi_3} s(\xi)d\xi \\ &= \int_0^{\xi_3}\left(a(\xi) + \frac{\sigma(\xi)}{j\omega}\right)d\xi \\ &= b(\xi_3) + \frac{\Delta(\xi_3)}{j\omega}\end{aligned} \tag{67}$$

where $a \geq 1$ and $\sigma \geq 0$. The effect of this stretching on a propagating wave can be seen by locally expanding the wave in terms of a generalized Wilcox expansion [146], [148], [149] showing that there is an induced exponential decay along the normal coordinate for $\sigma \geq 0$. Also, if $a \geq 1$, additional attenuation can be achieved for evanescent waves, if any.

The derivation of the CPML consists of substituting (67) in the system of Maxwell's equations expressed in curvilinear coordinates [150]. This leads to a system that is substantially different to the classic Maxwell's equations. For this reason, rather than to solve the system of Maxwell's equations in

[2]A Complex Frequency Shifted (CFS) formulation can be straightforwardly found [139], [147]. This presents some benefits for the attenuation of low frequency waves.

curvilinear coordinates, we recover the original system introducing an anisotropic medium. This leads to the formulation of the anisotropic and conformal PMLs.

1) Anisotropic Conformal PML: Let us start by introducing a new set of fields $\tilde{E}_i$ and $\tilde{H}_i$ defined as

$$\tilde{E}_1 = \frac{\tilde{h}_1}{h_1}E_1, \quad \tilde{E}_2 = \frac{\tilde{h}_2}{h_2}E_2, \quad \tilde{E}_3 = sE_3 \tag{68}$$

$$\tilde{H}_1 = \frac{\tilde{h}_1}{h_1}H_1, \quad \tilde{H}_2 = \frac{\tilde{h}_2}{h_2}H_2, \quad \tilde{H}_3 = sH_3 \tag{69}$$

with

$$\tilde{h}_1 = \frac{\tilde{r}_1}{r_{01}} \tag{70}$$

$$\tilde{h}_2 = \frac{\tilde{r}_2}{r_{02}} \tag{71}$$

$$\tilde{h}_3 = 1 \tag{72}$$

and $\tilde{r}_i = r_{0i} + \tilde{\xi}_3$.

By introducing these new fields into the system of equations described previously, we recover a Maxwellian system of equations in curvilinear coordinates, but now for an anisotropic medium whose constitutive parameters are given by $\bar{\bar{\mu}} = \mu\bar{\bar{\Lambda}}$ and $\bar{\bar{\varepsilon}} = \varepsilon\bar{\bar{\Lambda}}$, with

$$\bar{\bar{\Lambda}} = \mathbf{u}_1\mathbf{u}_1\left(\frac{sh_1\tilde{h}_2}{\tilde{h}_1h_2}\right) + \mathbf{u}_2\mathbf{u}_2\left(\frac{s\tilde{h}_1h_2}{h_1\tilde{h}_2}\right) + \mathbf{u}_3\mathbf{u}_3\left(\frac{\tilde{h}_1\tilde{h}_2}{sh_1h_2}\right) \tag{73}$$

So we can write Maxwell's equations in PML media as

$$\nabla \times \vec{E} = -\bar{\bar{\mu}}j\omega\vec{H} \tag{74}$$

$$\nabla \times \vec{H} = \bar{\bar{\varepsilon}}j\omega\vec{E} \tag{75}$$

This means that we can achieve a reflection-less absorption of electromagnetic waves incident on a smooth, concave surface with an anisotropic constitutive tensor over the volume spanning S between S'.

2) Cartesian PML: The Cartesian PML is a particular case of the system described in VII-A1. In this case we have that $r_{01} = r_{02} = \infty$, so that $\tilde{h}_1 = \tilde{h}_2 = 1$. Let us assume that the normal to our surface S is oriented towards the $+z$ axis, and therefore, $\mathbf{u}_1 = \mathbf{u}_x$, $\mathbf{u}_2 = \mathbf{u}_y$ and $\mathbf{u}_3 = \mathbf{u}_z$. Let us consider that $s = s_z(z) = 1 + \sigma_z(z)/(j\omega)$ for attenuation in the z direction. The $\sigma_z(z)$ profile is taken to minimize the reflections [12], [138] that for the parabolic case takes the form

$$\sigma_z(z) = \sigma_{\max}\left(\frac{z}{\Delta z}\right)^2 \tag{76}$$

Δz being the thickness of the PML. Uniaxial and biaxial PMLs can be considered a special case of the triaxial PML. By writing them explicitly we see that we need only certain DOFs depending on the direction, a fact that can be used with nodal basis to reduce the storage needs as mentioned in Section IV-F2.

a) Uniaxial Cartesian PML: For uniaxial PMLs, (73) reduces to

$$\bar{\bar{\Lambda}}_z = \mathbf{u}_x\mathbf{u}_x s_z + \mathbf{u}_y\mathbf{u}_y s_z + \mathbf{u}_z\mathbf{u}_z\frac{1}{s_z} \tag{77}$$

The x component of Faraday's law in PML media (74) is

$$-[\nabla \times \vec{E}]_x = \mu s_z j\omega\vec{H}_x = j\omega\mu\vec{H}_x + \sigma_z\mu\vec{H}_x \tag{78}$$

or, in the time domain

$$\mu\partial_t\vec{H}_x = -[\nabla \times \vec{E}]_x - \sigma_z\mu\vec{H}_x \tag{79}$$

and similarly for the y component. The z component is,

$$\begin{aligned} -[\nabla \times \vec{E}]_z &= \mu\frac{j\omega\vec{H}_z}{s_z} \\ &= \mu\frac{j\omega\vec{H}_z + \sigma_z\vec{H}_z - \sigma_z\vec{H}_z}{1 + \frac{\sigma_z}{j\omega}} \\ &= \mu j\omega\vec{H}_z - \mu\frac{\sigma_z j\omega\vec{H}_z}{j\omega + \sigma_z} \\ &= \mu j\omega\vec{H}_z + \mu\vec{M}_z - \mu\sigma_z\vec{H}_z \end{aligned} \tag{80}$$

with

$$j\omega\vec{M}_z = -\sigma_z\vec{M}_z + \sigma_z^2\vec{H}_z \tag{81}$$

which, in the time domain

$$\begin{aligned} \mu\partial_t\vec{H}_z &= -[\nabla \times \vec{E}]_z - \mu\vec{M}_z + \mu\sigma_z\vec{H}_z \\ \partial_t\vec{M}_z &= -\sigma_z\vec{M}_z + \sigma_z^2\vec{H}_z \end{aligned} \tag{82}$$

Similar equations can be obtained for Ampere's law (75) for PML media. Eq. (82) shows the need of introducing a new equation, called Auxiliary Differential Equation (ADE) that governs the behavior of a polarization current, $\vec{M}$. This is a common feature between PMLs and Dispersive materials, described in Section VII-B.

b) Biaxial Cartesian PML: When stretching in x and y directions, the tensor in (73) can be expressed as,

$$\begin{aligned} \bar{\bar{\Lambda}}_{x,y} &= \bar{\bar{\Lambda}}_x(x)\bar{\bar{\Lambda}}_y(y) \\ &= \frac{s_y}{s_x}\mathbf{u}_x\mathbf{u}_x + \frac{s_x}{s_y}\mathbf{u}_y\mathbf{u}_y + s_xs_y\mathbf{u}_z\mathbf{u}_z \end{aligned} \tag{83}$$

The x component of Faraday's law, after following a similar procedure as in the previous section, is

$$\mu\partial_t\vec{H}_x = -[\nabla \times \vec{E}]_x - \mu(\sigma_y - \sigma_x)\vec{H}_x - \mu\vec{M}_x \tag{84}$$

$$\partial_t\vec{M}_x = -\sigma_x(\sigma_y - \sigma_x)\vec{H}_x - \sigma_x\vec{M}_x \tag{85}$$

the y component can be obtained by switching x and y components in the previous expression. The z component is

$$\begin{aligned} \partial_t\vec{H}_z &= -[\nabla \times \vec{E}]_z - \mu(\sigma_x + \sigma_y)\vec{H}_z - \mu\vec{M}_z \\ \partial_t\vec{M}_z &= \sigma_x\sigma_y\vec{M}_z \end{aligned} \tag{86}$$

And similarly expressions can be obtained for Ampere's law (75).

c) Triaxial Cartesian PML: The tensor (73) stretched on all directions arise the most general form

$$\bar{\bar{\Lambda}}_{x,y,z} = \bar{\bar{\Lambda}}_x(x)\bar{\bar{\Lambda}}_y(y)\bar{\bar{\Lambda}}_z(z) \tag{87}$$

The x component of Faraday's law can be expressed as,

$$\begin{aligned} -[\nabla \times \vec{E}]_x &= j\omega\mu\frac{s_zs_y}{s_x}\vec{H}_x \\ &= j\omega\mu\vec{H}_x + \mu(\sigma_z + \sigma_y - \sigma_x)\vec{H}_x \\ &\quad + \mu\frac{(\sigma_z - \sigma_x)(\sigma_y - \sigma_x)}{j\omega + \sigma_x}\vec{H}_x \\ &= j\omega\mu\vec{H}_x + \mu(\sigma_z + \sigma_y - \sigma_x)\vec{H}_x + \mu\vec{M}_x \end{aligned} \tag{88}$$

with

$$j\omega\vec{M}_x = -\sigma_x\vec{M}_x + (\sigma_z - \sigma_x)(\sigma_y - \sigma_x)\vec{H}_x \tag{89}$$

which in the time domain

$$\begin{aligned}\mu\partial_t\vec{H}_x &= -[\nabla\times\vec{E}]_x - \mu(\sigma_z+\sigma_y-\sigma_x)\vec{H}_x - \mu\vec{M}_x\\ \partial_t\vec{M}_x &= -\sigma_x\vec{M}_x + (\sigma_z-\sigma_x)(\sigma_y-\sigma_x)\vec{H}_x\end{aligned} \tag{90}$$

And similarly for the y and z components and Ampere's law (75).

3) Constant/Varying conductivities: The equations (82), (86), and (90) together with the conductivity profile (76) require us to define and store additional mass matrices that are modified by the conductivities involved. This is a substantial amount of additional memory that will also impact the performance of the simulation. For certain cases, the benefits of using the conductivity profile (76) are clear as was found in [12], [138]. If, rather than using a varying conductivity we choose a constant profile, there is no need to compute additional mass matrices and equations (82), (86), and (90) are significantly simplified. This, however, results in an increase in the energy reflected which may be a factor, depending on the application.

Note also that the PMLs may have some stability problems if we are not careful when choosing large values for conductivity [123], particularly in time-integration schemes with closed stability regions (shown in Table IV). A discussion on this issue will be carried out in section VII-B2.

B. Dispersive materials

The simulation of dispersive media requires the introduction of new DOFs. This makes DGTD particularly well-suited for the simulation of these media because, as discussed in Section IV, its higher convergence properties let us attain a better accuracy per DOF than other techniques. There are many models available to model dispersive media. The three most common are the Debye's [67], [151], [152], Drude's [107], [153]–[155] and Lorentz's [156]–[158] models. These models can present multiple poles that arise from theoretical arguments of material electromagnetic properties. In this Section, we show how to adapt the complex-conjugate pole-residue pairs model (CCPR) proposed and demonstrated in [159], [160] for the FDTD technique. An interesting feature of the CCPR model is that it encompasses the other three models as they can be expressed as particular cases of it. Another important feature of the CCPR model is that we can use already-known and freely-available tools to obtain optimal poles and residue pairs for a given set of permittivities or permeabilities [161]–[163].

1) General Formulation: Let us consider the source-free Maxwell's equations (1) and (2) under the assumption that only homogeneous and isotropic media are present and therefore, electromagnetic parameters can be assumed to be local and spatially constant. When equations (1) and (2) are stated for dispersive media in the FD, the permittivity is a frequency-dependent magnitude. Following the approach of [159] we can model $\varepsilon(\omega)$ as

$$\varepsilon(\omega) = \varepsilon_0\varepsilon_\infty + \varepsilon_0\sum_{r=1}^{R}\left[\chi_r(\omega) + \chi_r'(\omega)\right] \tag{91}$$

with

$$\chi_r(\omega) = \frac{c_r}{j\omega - a_r} \quad \text{and} \quad \chi_r'(\omega) = \frac{c_r^*}{j\omega - a_r^*} \tag{92}$$

where $\varepsilon_\infty \in \mathbb{R}$ is the permittivity at an infinite frequency and c_r, $a_r \in \mathbb{C}$ are parameters chosen such that (91) fits the actual permittivity data of the material to be modeled. This fit can be done using the vector-fitting (VF) routines proposed in [161]–[163]. The number of residues and poles pairs, R, necessary to obtain a good approximation depends on the complexity of the actual $\varepsilon(\omega)$. A necessary condition to ensure that ε is stable and causal is that the real part of a_r is negative.

Introducing model (91) into equation (2),

$$\varepsilon_0\varepsilon_\infty\partial_t\vec{E} = \vec{\nabla}\times\vec{H} - \sigma\vec{E} - \sum_{r=1}^{R}\left(\partial_t\vec{P}_r + \partial_t\vec{P}_r'\right) \tag{93}$$

with

$$\vec{P}_r = \varepsilon_0\chi_r\vec{E} \quad \text{and} \quad \vec{P}_r' = \varepsilon_0\chi_r'\vec{E} \tag{94}$$

Considering also that if $\vec{E} \in \mathbb{R}$ then $\vec{P}_r' = \vec{P}_r^*$ we can finally rewrite (1) and (93) as a system of $R+2$ coupled PDEs.

$$\begin{aligned}\partial_t\vec{E} &= \frac{1}{\varepsilon_0\varepsilon_\infty}\left[\vec{\nabla}\times\vec{H} - \sigma\vec{E} - 2\sum_{r=1}^{R}\Re[a_r\vec{P}_r + \varepsilon_0 c_r\vec{E}]\right]\\ \partial_t\vec{H} &= -\frac{1}{\mu}\vec{\nabla}\times\vec{E}\\ \partial_t\vec{P}_r &= a_r\vec{P}_r + \varepsilon_0 c_r\vec{E} \qquad \forall r = 1,\ldots,R\end{aligned} \tag{95}$$

With this formulation, the most commonly used dispersive-media models can be obtained as particular cases:

- A purely conductive media can be modeled using a single residue-pole ($R=1$) pair with $a_0 = 0$ and $c_0 = \sigma/(2\varepsilon_0)$. This is equivalent to adding a conductivity term $\sigma\vec{E}$ into equation (2).
- Poles of a Debye's model can be obtained with $c_r = \Delta\varepsilon_r/(2\tau_r)$ and $a_r = -1/\tau_r$. With $\Delta\varepsilon_r$ and τ_r being the parameters characterizing the Debye poles [132].
- Similarly for Lorentz's media we have that $c_r = j\Delta\varepsilon_r\omega_r^2/(2\sqrt{\omega_r^2 - \delta_r^2})$ and $a_r = -\delta_r - j\sqrt{\omega_r^2 - \delta_r^2}$. With $\Delta\varepsilon_r$, δ_r, and τ_r being the parameters characterizing the Lorentz poles [132].

2) Stability of dispersive models: The stability conditions for dispersive media have been studied by several authors [123], [157], [164] finding that the DG semi-discretized scheme is stable for any physically stable model. When we introduce dispersion models, we find that the original eigenvalues that we obtained (28) are affected by the new equations in (95). The new eigenvalues or the modification of the existing ones may make them move out of the stability regions (Fig. 6) forcing us to reduce h_t to ensure the stability of the scheme. For dispersive media [152], [165] and [157] show that the DGTD and CGTD schemes with LF2 time integration schemes are stable and that their solutions converge. This happens because the leap-frog schemes are only unstable depending on the imaginary part of the eigenvalues present in Maxwell's equations (95) as discussed in Section V-A. However, when we apply the LSERK4 scheme introduced in section V-B the new eigenvalues may lead to unstable schemes if the modified eigenfrequencies fall out of the closed stability region.

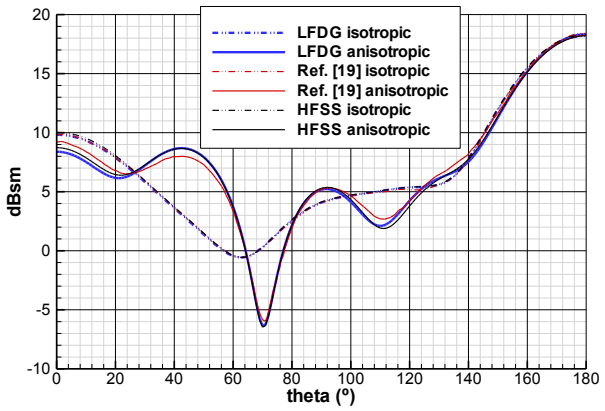

Fig. 9: Bistatic RCS of an isotropic/anisotropic sphere ($D = 1.2\lambda$ and $\lambda = 1.0m$). LFDG results are compared to those appearing in [167], and computed with Ansoft HFSS.

C. Anisotropic materials

The DGTD method can be straightforwardly extended to anisotropic materials [11], [12], [96], [166]. Substituting ε and μ in (1) and (2) with electric permittivity and magnetic permeability symmetric positive-definite tensors $\bar{\bar{\varepsilon}}$ and $\bar{\bar{\mu}}$.

We can express $\bar{\bar{\varepsilon}}$ and $\bar{\bar{\mu}}$, and their inverses, in a local base of vectors. Following an operation splitting method similar as was done in section IV-B, we can again derive a one-dimensional Riemann problem to deduce new conditions for the numerical fluxes (20). However, the fact that we are using tensors leads us to expressions for two matrices, *impedance* ($\bar{\bar{Z}}_2$) and *admittance* ($\bar{\bar{Y}}_2$), which play a role equivalent to the scalar impedance (Z) and admittance (Y) magnitudes defined for the isotropic case. Finally, $\bar{\bar{Z}}_2$ and $\bar{\bar{Y}}_2$ are used as the impedance values indicated in table II to account for the anisotropic nature of the media. The rest of the scheme is also affected by the tensorial nature of $\bar{\bar{\varepsilon}}$ and $\bar{\bar{\mu}}$ but their effect is simply to scale the mass matrices (14) depending on the tensor values.

Results for the RCS of an anisotropic sphere are shown in Fig. 9 (from [11]). In this problem, a sphere is illuminated with a linearly polarized plane wave. The bistatic RCS is computed at a frequency for which the diameter is $D = 1.2\lambda$, with λ being the wavelength. The results are compared with a reference case [167] and with the solution provided by the Ansoft HFSS commercial software. The maximum difference found is 0.35 dB, therefore resulting in a good agreement.

VIII. Subcell models

Through a modification of the numerical flux conditions we can model a wide variety of phenomenons such as lumped elements, multi-port networks, or thin layers.

A. Lumped elements

The modeling of passive lumped elements such as resistors, capacitors, and inductors and general combinations of them has been studied in [168]–[170], a generalization of the previous works for multi-port networks is carried out in [65], [171]. Lumped elements can also be seen as special cases of thin layers, which are introduced in the next section.

B. Thin layers

Thin layers of any material, including anisotropic and dispersive media, are described in [172]–[174] for the FDTD method. Specifically for DGTD, a simple resistive layer was introduced in [64] and a rigorous formulation and validation, suitable also for curved geometries, is shown in [96] and [175]. To model thin layers, we use a Surface Impedance Boundary Condition (SIBC) that reproduces its behavior. Note also that an SIBC defined over a free surface can also be regarded as a two-port network model (see Fig. 10).

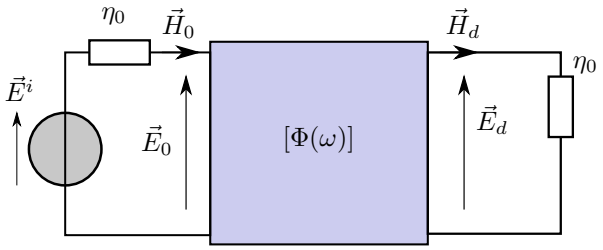

Fig. 10: Two-port representation of the air-embedded panel illuminated by a TEM plane wave.

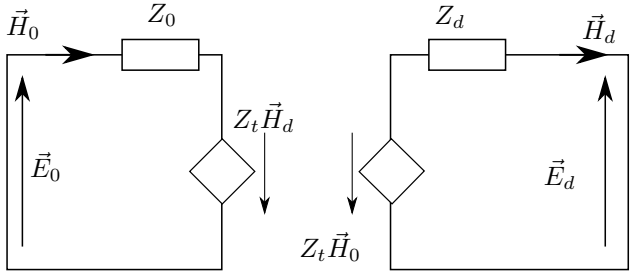

Fig. 11: Magnetic field-controlled circuit representation of a thin layer.

Let us suppose that an indefinite panel embedded in air is illuminated by a normally-incident TEM plane wave. An equivalent circuit of this setup is shown in Fig. 11 in which $\vec{E}_0$, $\vec{E}_d$, $\vec{H}_0$ and $\vec{H}_d$ are the components of the electric and magnetic fields which are tangential to the external faces (0 and d) of the slab, respectively. Using a two-port transmission line formalism we can deduce that the following relationship between the field components

$$\begin{pmatrix} \vec{E}_0(\omega) \\ \vec{H}_0(\omega) \end{pmatrix} = [\Phi(\omega)] \begin{pmatrix} \vec{E}_d(\omega) \\ \vec{H}_d(\omega) \end{pmatrix} \tag{96}$$

with

$$\Phi_{11}(\omega) = \Phi_{22}(\omega) = \cosh(\gamma d) \tag{97}$$
$$\Phi_{12}(\omega) = \eta \sinh(\gamma d) \tag{98}$$
$$\Phi_{21}(\omega) = \eta^{-1} \sinh(\gamma d) \tag{99}$$

with η and γ being the intrinsic impedance and the propagation constant, respectively. Note that these expressions are derived from ε and μ which can depend on ω, as the ones presented in Section VII-B.

Matrix equation (96) can be transformed, using widely known two-port network relationships [176], into the following equivalent magnetic field-controlled (MFC) formulation:

$$\underbrace{\begin{bmatrix}\vec{E}_0\\ \vec{E}_d\end{bmatrix}}_{\tilde{\vec{E}}} = \underbrace{\begin{bmatrix}Z_0 & -Z_t\\ Z_t & -Z_d\end{bmatrix}}_{\tilde{\mathcal{Z}}(\omega)} \underbrace{\begin{bmatrix}\vec{H}_0\\ \vec{H}_d\end{bmatrix}}_{\tilde{\vec{H}}} \tag{100}$$

Fig. 11 shows the sketch of the circuit model of (100) in which the dependence of the electric field at the one side of the slab from the magnetic field at the other one is represented by MFC electric-field sources. Note that for non-symmetrical multi-layered slabs the coefficients Φ_{11} and Φ_{22} are not coincident, even if matrix $[\Phi(\omega)]$ always satisfies the reciprocity condition; therefore, the impedances Z_0 and Z_d can assume different values. The $\tilde{\mathcal{Z}}$ can be decomposed using a VF technique such as the one we used in Section VII-B, using, for instance, the routines provided by [161]–[163]

$$\tilde{\mathcal{Z}}(\omega) = \tilde{\mathcal{Z}}_\infty + \sum_{p=1}^{P} \frac{\tilde{\mathcal{Z}}_p}{j\omega - a_p} \tag{101}$$

being $\tilde{\mathcal{Z}}_\infty$ and $\tilde{\mathcal{Z}}_p$ an approximation of the impedance matrix of the medium. With this decomposition $\tilde{E}$ can be expressed as

$$\tilde{\vec{E}}(\omega) = \tilde{Q}_\infty(\omega) + \sum_{p=1}^{P} \tilde{Q}_p(\omega) \tag{102}$$

with

$$\tilde{Q}_\infty = \begin{bmatrix}\vec{Q}_{0,\infty}\\ \vec{Q}_{d,\infty}\end{bmatrix} = \tilde{\mathcal{Z}}_\infty \tilde{\vec{H}} \tag{103}$$

and

$$\tilde{Q}_p = \begin{bmatrix}\vec{Q}_{0,p}\\ \vec{Q}_{d,p}\end{bmatrix} = \tilde{\mathcal{Z}}_p \tilde{\vec{H}} \tag{104}$$

Making use of the ADE formalism, the infinity frequency term is

$$\tilde{Q}_\infty(t) = \tilde{\mathcal{Z}}_\infty \tilde{\vec{H}}(t) \tag{105}$$

The frequency dependent terms arise to P new differential equations

$$\partial_t \tilde{Q}_p = a_p \tilde{Q}_p + \tilde{\mathcal{Z}} \tilde{\vec{H}}(t) \tag{106}$$

that are solved similarly as we did in Section VII-B for dispersive materials. The calculated electric fields are used, similarly as was done in (23), (24), and (25), to modify the jump terms (21) in the following way,

$$\begin{aligned}[[\vec{E}^h]]_{\text{SIBC},0} &= 2(\vec{E}^h - \vec{E}^h_0)\\ [[\vec{H}^h]]_{\text{SIBC},0} &= 0\end{aligned} \tag{107}$$

and similarly at the d side of the SIBC,

$$\begin{aligned}[[\vec{E}^h]]_{\text{SIBC},d} &= 2(\vec{E}^h - \vec{E}^h_d)\\ [[\vec{H}^h]]_{\text{SIBC},d} &= 0\end{aligned} \tag{108}$$

C. Thin wire geometries

Many common EMC problems often need the evaluation of currents flowing along cables. The typical approach is to model cables as thin wires that are split into segments located along the edges of the cells in the mesh [64]. For each segment, the currents and charges are evaluated following an implementation of the Holland formalism [177], [178]. These equations are discretized for each of the segments following a similar formalism as the one explained in section IV, but this time for a one-dimensional problem weakly coupled with our original semi-discretization [169].

A different approach is followed by [179] in which the region containing the thin wires is solved using the Time Domain Integral Equation that is then coupled with the DGTD algorithm by a modification of the numerical fluxes, similarly as was done in section VI-A for plane waves.

IX. Computational implementation

In this section, we present some final remarks regarding the computational implementation of a few of the techniques previously described.

A. Geometrical discretization

An important aspect of an efficient simulation is the capability to generate complex meshes. This requirement is fulfilled by most of the commercial CAD tools.

The tool SEMBA, that we have developed, uses GiD for pre- and post-processing. GiD [101] is a commercial tool that allows pre-processing of geometries with CAD-importing capabilities. These geometries can be meshed in a variety of ways, including structured and semistructured meshes, linear or quadratic elements, and several types of elements (tetrahedrons, hexahedrons, prisms, ...). The program permits a high degree of customization that allows users to develop their own problem types. Additionally, the results obtained can be easily visualized, and several post-processing tools are also offered.

There are many other applications that can offer solutions for obtaining meshes. Among the open source tools, we highlight Gmsh [100] and OpenFoam [180].

B. Preprocessing

To increase the efficiency of the computations and implement certain capabilities, it is necessary to perform some pre-processing tasks. These tasks are usually optional as they depend on the capabilities implemented in the solver.

1) Selection of basis functions: An *a priori* hp-refinement heuristic strategy consists of choosing the size of the mesh, and the order of the basis function in each tetrahedron [12]. The target is to ensure a given accuracy level, minimizing the computational cost. The selection of the mesh size has to be made in the mesh-generation process, since there is an optimum element size that minimizes the computational cost for a required accuracy. In real meshes, the element sizes vary throughout the computational domain, and the accuracy is finally adjusted with the selection of the order p. This allows

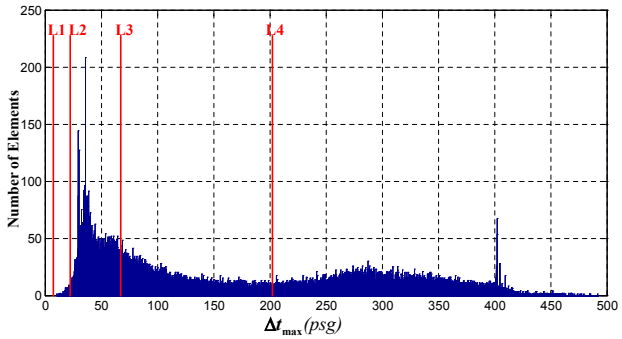

(a) Example of distribution of time steps in a real problem (described in [10]). The choice of the time step and the time steps of different levels have been included in the plot. The estimated average time step was 88.5 ps, compared to the minimum 10.5 ps [12].

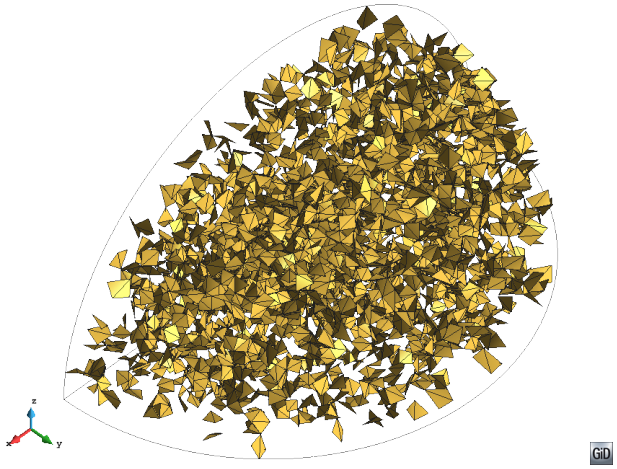

(b) Elements evolved with the doubling of the minimum timestep (Tier 1) using an LTS technique for LF2 [20].

Fig. 12: Assortment of tiers for the use of a LTS technique.

us to employ a higher-order basis for larger tetrahedrons, and lower orders for smaller ones. This approach can also combine gradient spaces of reduced order $p-1$, with rotational spaces of complete order p [82].

It bears noting that smaller elements need shorter timesteps, but if lower orders are used in these elements, the stability condition is also relaxed. The combination and mixing of different orders of the basis functions depending on element size makes the timestep among all the elements more homogeneous, thereby reducing the number of levels required for the LTS algorithm.

2) LTS Level classification: The local time-stepping strategy described in Section V-C1 requires a classification of all the elements according to their maximum timestep. Fig. 12 illustrates the distribution of the timesteps for the elements in a real problem. As there are usually some costs associated with the buffering zones between time tiers [12], [20], [22], [126], the minimum timestep can be actually tuned to provide a maximum average timestep.

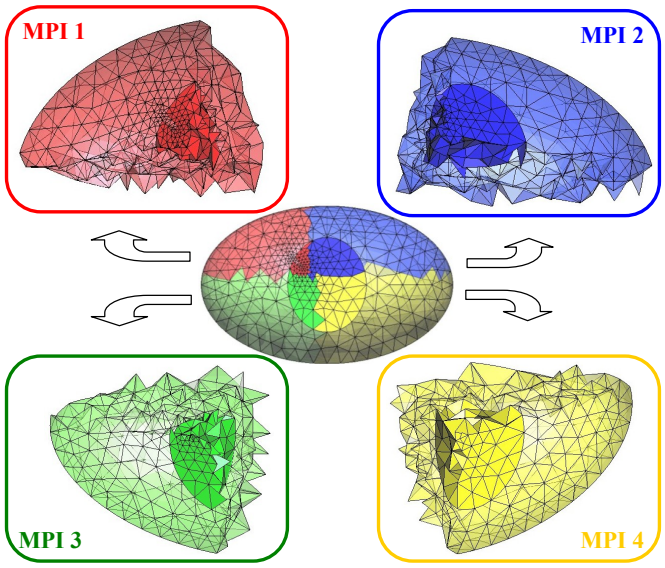

Fig. 13: Distribution of the mesh among the different MPI processes.

C. Parallelization

One key advantage of discontinuous Galerkin methods is their simplicity for the parallelization in memory-distributed hardware architecture, a feature that arises from its explicitness. This allows us to make use of the Message Passing Interface (MPI) standard [105], [107], [181] or the GPU (CUDA/OpenCL) [120], [182], [183]. The DGTD method exhibits great boosts in performance thanks to its memory locality, the regularity of access patterns and the high arithmetic intensity [183]. There are several ways to perform the partitioning of the mesh carried out during the pre-processing stage. The simplest way is to manually define regions that are handled by the different processes (Fig. 13). However, as pointed out in [120], this may result in a load unbalance that drastically reduces the efficiency. To solve this issue, the ParMetis library [184] can be used to partition the mesh, assigning different weights to the cells depending on the number of arithmetic operations they need. ParMetis can also be configured to provide the partition with the minimum interface, to optimize the interprocess communication. Other techniques developed for FDTD can also be used to reduce the number of interprocess communications [185].

ACKNOWLEDGMENTS

The authors wish to gratefully thank Prof. S. Gedney for being the origin of this fruitful line of research at the UGR group. Also to Prof. Fernando L. Teixeira, Dr. X. Ferrieres, Dr. J. P. Parmantier, and Prof. Stephane Lanteri for their direct and indirect contributions to this manuscript. This work has been partially funded through the European Community's Seventh Framework Programme FP7/2007-2013, under grant agreement no 205294 (HIRF-SE project), by the National Projects TEC2010-20841-C04-04, TEC2013-48414-C3-01, CSD2008-00068, P09-TIC-5327, P12-TIC-1442, and by the GENIL excellence network.

REFERENCES

[1] C. Dawson and J. Proft, "Coupling of continuous and discontinuous Galerkin methods for transport problems," *Computer Methods in Applied Mechanics and Engineering*, vol. 191, no. 29–30, pp. 3213 – 3231, 2002.

[2] T. C. Warburton and G. E. Karniadakis, "A discontinuous Galerkin method for the viscous MHD equations," *J. Comput. Phys.*, vol. 152, pp. 608–641, July 1999.

[3] Y. Xu and C.-W. Shu, "Local discontinuous Galerkin methods for nonlinear Schrödinger equations," *Journal of Computational Physics*, vol. 205, no. 1, pp. 72 – 97, 2005.

[4] M. Dumbser, M. Käser, and E. F. Toro, "An arbitrary high-order discontinuous Galerkin method for elastic waves on unstructured meshes - v. local time stepping and p-adaptivity," *Geophysical Journal International*, vol. 171, no. 2, pp. 695–717, 2007.

[5] S. Petersen, C. Farhat, and R. Tezaur, "A space–time discontinuous Galerkin method for the solution of the wave equation in the time domain," *International Journal for Numerical Methods in Engineering*, vol. 78, no. 3, pp. 275–295, 2009.

[6] "SEMBA, simulador electromagnetico de banda ancha." http://www.ugrfdtd.es.

[7] J. Alvarez, L. Angulo, M. Fernandez Pantoja, A. Rubio Bretones, and S. Garcia, "Source and boundary implementation in vector and scalar DGTD," *Antennas and Propagation, IEEE Transactions on*, vol. 58, no. 6, pp. 1997 –2003, 2010.

[8] J. Alvarez, L. D. Angulo, S. G. Garcia, M. F. Pantoja, and A. R. Bretones, "A comparison between upwind/centered nodal/vector basis DGTD," in *IEEE International Symposium on Antennas and Propagation and CNC/USNC/URSI Radio Science Meeting*, 2010.

[9] L. D. Angulo, J. Alvarez, S. Garcia, A. R. Bretones, and R. G. Martin, "Discontinuous Galerkin time-domain method for GPR simulation of conducting objects," *Near Surface Geophysics*, vol. 9, pp. 257–263, 2011.

[10] J. Alvarez, L. D. Angulo, A. Rubio Bretones, and S. Garcia, "A spurious-free discontinuous Galerkin time-domain method for the accurate modeling of microwave filters," *Microwave Theory and Techniques, IEEE Transactions on*, vol. 60, no. 8, pp. 2359–2369, 2012.

[11] J. Alvarez, L. D. Angulo, A. Rubio Bretones, and S. Gonzalez Garcia, "3D discontinuous Galerkin time–domain method for anisotropic materials," *Antennas and Wireless Propagation Letters, IEEE*, vol. 11, pp. 1182–1185, 2012.

[12] J. Alvarez, *A Discontinuous Galerkin Finite Element Method for the Time-Domain Solution of Maxwell Equations*. PhD thesis, Universidad de Granada, 2013.

[13] J. Alvarez, L. D. Angulo, M. Bandinelli, H. Bruns, M. Francavilla, S. Garcia, R. Guidi, G. Gutierrez, C. Jones, M. Kunze, J. Martinaud, I. Munteanu, M. Panitz, J. Parmantier, P. Pirinoli, Z. Reznicek, G. Salin, A. Schroder, P. Tobola, and F. Vipiana, "HIRF interaction with metallic aircrafts. a comparison between TD and FD methods," in *Electromagnetic Compatibility (EMC EUROPE), 2012 International Symposium on*, pp. 1–6, 2012.

[14] J. Alvarez, L. D. Angulo, A. R. Bretones, and S. G. Garcia, "A comparison of the FDTD and LFDG methods for the estimation of HIRF transfer functions," in *Proceedings on Computational ElectroMagnetics And Electromagnetic Compatibility 2013 (CEMEMC13)*, 2013.

[15] J. Alvarez, L. D. Angulo, A. Bretones, M. Cabello, and S. Garcia, "A leap-frog discontinuous Galerkin time-domain method for HIRF assessment," *Electromagnetic Compatibility, IEEE Transactions on*, vol. 55, no. 6, pp. 1250–1259, 2013.

[16] J. Alvarez, P. E., G. G., A. M., F. S., C. A., R.-C. M., L. D. Angulo, and S. Gonzalez Garcia, "HIRF SE. desarrollo y validación de un entorno sintético de simulación para soporte en el diseño y certificación de aeronaves," in *DESEI+D*, 2013.

[17] G. Gutierrez, J. Alvarez, E. Pascual-Gil, M. Bandinelli, R. Guidi, V. Martorelli, M. Pantoja, M. Cabello, and S. Garcia, "HIRF virtual testing on the C-295 aircraft: On the application of a pass/fail criterion and the fsv method," *Electromagnetic Compatibility, IEEE Transactions on*, vol. PP, no. 99, pp. 1–10, 2013.

[18] J. Alvarez, J. M. Alonso-Rodriguez, H. Carbajosa-Cobaleda, M. R. Cabello, L. D. Angulo, R. Gomez-Martin, and S. G. Garcia, "DGTD for a class of low-observable targets: A comparison with mom and (2,2) FDTD," *IEEE Antennas and Wireless Propagation Letters*, vol. 13, pp. 241–244, 2014.

[19] J. Alvarez, L. D. Angulo, M. Cabello, A. R. Bretones, and S. G. Garcia, "An analysis of the leap-frog discontinuous Galerkin method for Maxwell's equations," *IEEE Transactions on Microwave Theory and Techniques*, vol. 62, pp. 197–207, February 2014.

[20] L. D. Angulo, J. Alvarez, F. Teixeira, M. Pantoja, and S. Garcia, "Causal-path local time-stepping in the discontinuous Galerkin method for Maxwell's equations," *Journal of Computational Physics*, vol. 256, pp. 678 – 695, 2014.

[21] L. D. Angulo, J. Alvarez, M. F. Pantoja, and S. G. Garcia, "An explicit nodal space-time discontinuous Galerkin method for Maxwell's equations," *IEEE Microwave and Wireless Components Letters*, Accepted.

[22] J. Alvarez, L. D. Angulo, A. Rubio Bretones, C. M. de Jong, and S. G. Garcia, "Efficient antenna modeling by DGTD," *IEEE Antennas and Propagation Magazine*, Submitted.

[23] L. D. Angulo, J. Alvarez, F. L. Teixeira, M. F. Pantoja, and S. G. Garcia, "A nodal hybrid continuous-discontinuous Galerkin time domain method for Maxwell's equations," *IEEE Transactions On Microwave Theory And Techniques*, Submitted.

[24] J. S. Hesthaven and T. Warburton, *Nodal Discontinuous Galerkin Methods: Algorithms, Analysis, and Applications*. Springer Publishing Company, Incorporated, 1st ed., 2007.

[25] J. S. Hesthaven and T. Warburton, "Discontinuous Galerkin methods for the time-domain Maxwell's equations: An introduction," *ACES Newsletter*, vol. 19, no. 1, pp. 10–29, 2004.

[26] J. Chen and Q. H. Liu, "Discontinuous Galerkin time-domain methods for multiscale electromagnetic simulations: A review," *Proceedings of the IEEE*, vol. 101, no. 2, pp. 242–254, 2013.

[27] K. Busch, M. Konig, and J. Niegemann, "Discontinuous Galerkin methods in nanophotonics," *Laser & Photonics Reviews*, vol. 5, no. 6, pp. 773–809, 2011.

[28] K.-P. Hwang, "Computational efficiency of Fang's fourth-order FDTD schemes," *Electromagnetics*, vol. 23, no. 2, pp. 89–102, 2003.

[29] S. Dey and R. Mittra, "A locally conformal finite-difference time-domain (FDTD) algorithm for modeling three-dimensional perfectly conducting objects," *Microwave and Guided Wave Letters, IEEE*, vol. 7, pp. 273–275, Sep 1997.

[30] C. D. Sarris, "Adaptive mesh refinement for time-domain numerical electromagnetics," *Synthesis Lectures on Computational Electromagnetics*, vol. 1, no. 1, pp. 1–154, 2007.

[31] J. Kim and F. Teixeira, "Parallel and explicit finite-element time-domain method for Maxwell's equations," *Antennas and Propagation, IEEE Transactions on*, vol. 59, no. 6, pp. 2350–2356, June.

[32] E. T. Chung and B. Engquist, "Optimal discontinuous Galerkin methods for wave propagation," *SIAM J. Numer. Anal.*, vol. 44, pp. 2131–2158, Sept. 2006.

[33] A. Taflove and S. C. Hagness, *Computational Electrodynamics The Finite-Differences Time Domain Method*. 2005.

[34] C. U. Kane Yee; University of California, Livermore, "Numerical solution of initial boundary value problems involving Maxwell's equations in isotropic media," *Antennas and Propagation, IEEE Transactions on*, vol. 14 Issue:3, pp. 302 – 307, 1966.

[35] S. Georgakopoulos, C. Birtcher, C. Balanis, and R. Renaut, "Higher-order finite-difference schemes for electromagnetic radiation, scattering, and penetration .1. theory," *Antennas and Propagation Magazine, IEEE*, vol. 44, pp. 134–142, Feb 2002.

[36] J. L. Young, "High-order, leapfrog methodology for the temporally dependent Maxwell's equations," *Radio Science*, vol. 36, no. 1, pp. 9–17, 2001.

[37] C. Fumeaux, D. Baumann, P. Leuchtmann, and R. Vahldieck, "A generalized local time-step scheme for efficient FVTD simulations in strongly inhomogeneous meshes," *Microwave Theory and Techniques, IEEE Transactions on*, vol. 52, pp. 1067–1076, March 2004.

[38] K. Sankaran, C. Fumeaux, and R. Vahldieck, "Cell-centered finite-volume-based perfectly matched layer for time-domain Maxwell system," *Microwave Theory and Techniques, IEEE Transactions on*, vol. 54, pp. 1269 – 1276, march 2006.

[39] D. Baumann, C. Fumeaux, R. Vahldieck, and E. Li, "Conformal perfectly matched absorber for finite-volume time-domain simulations," in *Electromagnetic Compatibility and 19th International Zurich Symposium on Electromagnetic Compatibility, 2008. APEMC 2008. Asia-Pacific Symposium on*, pp. 188 –191, May 2008.

[40] C. Bommaraju, W. Ackermann, and T. Weiland, "Convergence of error in FVTD methods on tetrahedral meshes in 3D," in *Applied Electromagnetics Conference (AEMC), 2009*, pp. 1–4, Dec 2009.

[41] J.-F. Lee, R. Lee, and A. Cangellaris, "Time-domain finite-element methods," *Antennas and Propagation, IEEE Transactions on*, vol. 45, no. 3, pp. 430–442, 1997.

[42] D. Lynch and K. Paulsen, "Time-domain integration of the Maxwell equations on finite elements," *Antennas and Propagation, IEEE Transactions on*, vol. 38, pp. 1933–1942, Dec 1990.

[43] J.-F. Lee and Z. Sacks, "Whitney elements time domain (WETD) methods," *Magnetics, IEEE Transactions on*, vol. 31, pp. 1325–1329, May 1995.

[44] J.-F. Lee, "WETD - a finite element time-domain approach for solving Maxwell's equations," *Microwave and Guided Wave Letters, IEEE*, vol. 4, pp. 11–13, Jan 1994.

[45] S. Gedney and U. Navsariwala, "An unconditionally stable finite element time-domain solution of the vector wave equation," *Microwave and Guided Wave Letters, IEEE*, vol. 5, pp. 332–334, Oct 1995.

[46] J.-M. Jin, M. Zunoubi, K. C. Donepudi, and W. C. Chew, "Frequency-domain and time-domain finite-element solution of Maxwell's equations using spectral Lanczos decomposition method," *Computer Methods in Applied Mechanics and Engineering*, vol. 169, no. 3–4, pp. 279 – 296, 1999.

[47] W. P. Carpes Jr, L. Pichon, and A. Razek, "A 3D finite element method for the modeling of bounded and unbounded electromagnetic problems in the time domain," *International Journal of Numerical Modelling: Electronic Networks, Devices and Fields*, vol. 13, no. 6, pp. 527–540, 2000.

[48] D. Jiao and J. M. Jin, "A general approach for the stability analysis of the time-domain finite-element method for electromagnetic simulations," *IEEE Transactions on Antennas and Propagation*, vol. 50, pp. 1624–1632, November 2002.

[49] D. Jiao and J. M. Jin, "Three-dimensional orthogonal vector basis functions for time-domain finite element solution of vector wave equations," *IEEE Transactions on Antennas and Propagation*, vol. 51, pp. 59–65, January 2003.

[50] Z. Lou and J.-M. Jin, "Modeling and simulation of broad-band antennas using the time-domain finite element method," *Antennas and Propagation, IEEE Transactions on*, vol. 53, pp. 4099–4110, Dec 2005.

[51] R. Wang, H. Wu, A. C. Cangellaris, and J. M. Jin, "Incorporation of a feed network into the time-domain finite-element modeling of antenna arrays," *IEEE Transactions on Antennas and Propagation*, vol. 56, pp. 2599–2612, August 2008.

[52] R. A. Chilton and R. Lee, "The discrete origin of FETD-Newmark late time instability, and a correction scheme," *J. Comput. Phys.*, vol. 224, pp. 1293–1306, June 2007.

[53] R. N. Rieben, G. H. Rodrigue, and D. A. White, "A high order mixed vector finite element method for solving the time dependent Maxwell equations on unstructured grids," *Journal of Computational Physics*, vol. 204, pp. 490–519, 2005.

[54] B. He and F. L. Teixeira, "Sparse and explicit FETD via approximate inverse Hodge (mass) matrix," *IEEE Microwave and Wireless Components Letters*, vol. 16, pp. 348–350, June 2006.

[55] B. He and F. L. Teixeira, "Differential forms, Galerkin duality, and sparse inverse approximations in finite element solutions of Maxwell equations," *IEEE Transactions on Antennas and Propagation*, vol. 55, pp. 1359–1368, May 2007.

[56] B. Donderici and F. Teixeira, "Conformal perfectly matched layer for the mixed finite element time-domain method," *Antennas and Propagation, IEEE Transactions on*, vol. 56, no. 4, pp. 1017 –1026, 2008.

[57] B. Donderici and F. L. Teixeira, "Mixed finite-element time-domain method for transient Maxwell equations in doubly dispersive media," *IEEE Transaction on Microwave Theory and Techniques*, vol. 56, pp. 113–120, January 2008.

[58] R. S. Chen, L. Du, Z. Ye, and Y. Yang, "An efficient algorithm for implementing the Crank-Nicolson scheme in the mixed finite-element time-domain method," *IEEE Transaction on Antennas and Propagation*, vol. 57, pp. 3216–3222, October 2009.

[59] J. S. Hesthaven and T. Warburton, "High-order nodal discontinuous Galerkin methods for the Maxwell eigenvalue problem," *Philosophical Transactions of the Royal Society of London. Series A:Mathematical, Physical and Engineering Sciences*, vol. 362, no. 1816, pp. 493–524, 2004.

[60] E. Miller, "A selective survey of computational electromagnetics," *Antennas and Propagation, IEEE Transactions on*, vol. 36, pp. 1281–1305, Sep 1988.

[61] S. Dosopoulos and J.-F. Lee, "Interior penalty discontinuous Galerkin finite element method for the time-dependent first order Maxwell's equations," *Antennas and Propagation, IEEE Transactions on*, vol. 58, no. 12, pp. 4085 –4090, 2010.

[62] S. Descombes, S. Lanteri, and L. Moya, "Locally implicit time integration strategies in a discontinuous Galerkin method for Maxwell's equations," *Journal of Scientific Computing*, vol. 56, no. 1, pp. 190–218, 2013.

[63] M. D'Amore, "C27J airframe lighting certification using CEM," in *EMC Europe 2010 Wroclaw*.

[64] L. Pebernet, X. Ferrieres, S. Pernet, F. Rogier, and P. Degond, "A discontinuous Galerkin method to solve electromagnetic problems," *IET Conference Publications*, vol. 2008, no. CP537, pp. 96–97, 2008.

[65] P. Li and L. J. Jiang, "Integration of arbitrary lumped multiport circuit networks into the discontinuous Galerkin time-domain analysis," *Microwave Theory and Techniques, IEEE Transactions on*, vol. 61, no. 7, pp. 2525–2534, 2013.

[66] Z. Lou and J.-M. Jin, "An accurate waveguide port boundary condition for the time-domain finite-element method," *Microwave Theory and Techniques, IEEE Transactions on*, vol. 53, no. 9, pp. 3014–3023, 2005.

[67] T. Lu, W. Cai, and P. Zhang, "Discontinuous galerkin time-domain method for GPR simulation in dispersive media," *Geoscience and Remote Sensing, IEEE Transactions on*, vol. 43, no. 1, pp. 72 – 80, 2005.

[68] B. Cockburn, G. E. Karniadakis, and C.-W. Shu, *Discontinuous Galerkin Methods*. Springer, 2000.

[69] C.-W. Shu, "Discontinuous Galerkin methods: general approach and stability." 2009.

[70] R. LeVeque, *Finite Volume Methods for Hyperbolic Problems*. Cambridge Texts in Applied Mathematics, Cambridge University Press, 2002.

[71] D. Sarmany, M. A. Botchev, and J. J. Vegt, "Dispersion and dissipation error in high-order Runge-Kutta discontinuous Galerkin discretisations of the Maxwell equations," *J. Sci. Comput.*, vol. 33, pp. 47–74, October 2007.

[72] M. Ainsworth, "Dispersive and dissipative behaviour of high order discontinuous Galerkin finite element methods," *J. Comput. Phys.*, vol. 198, pp. 106–130, July 2004.

[73] M. Ainsworth, P. Monk, and W. Muniz, "Dispersive and dissipative properties of discontinuous Galerkin finite element methods for the second-order wave equation," *Journal of Scientific Computing*, vol. 27, no. 1-3, pp. 5–40, 2006.

[74] E. Montseny, S. Pernet, X. Ferriéres, and G. Cohen, "Dissipative terms and local time-stepping improvements in a spatial high order discontinuous Galerkin scheme for the time-domain Maxwell's equations," *J. Comput. Phys.*, vol. 227, pp. 6795–6820, July 2008.

[75] J. Nedelec, *Acoustic and Electromagnetic Equations: Integral Representations for Harmonic Problems*. No. v. 144 in Acoustic and electromagnetic equations: integral representations for harmonic problems, Springer, 2001.

[76] K. Sankaran, *Accurate domain truncation techniques for time-domain conformal methods*. PhD thesis, ETH Zurich, 2007.

[77] S. Sherwin, "Dispersion analysis of the continuous and discontinuous Galerkin formulations.," in *in International Symposium on Discontinuous Galerkin Methods*, pp. 425–431, Springer, 1999.

[78] N. N. R. J. Descloux, Jean, "On spectral approximation. part 1. the problem of convergence," *ESAIM: Mathematical Modelling and Numerical Analysis - Modélisation Mathématique et Analyse Numérique*, vol. 12, no. 2, pp. 97–112, 1978.

[79] P. P. Silvester and R. L. Ferrari, *Finite elements for electrical engineers*. Cambridge University Press, third ed., 1996.

[80] J. Jin, *The Finite Element Method in Electromagnetics*. Wiley-Interscience, 1993.

[81] D. Sun, J. Manges, X. Yuan, and Z. Cendes, "Spurious modes in finite-element methods," *Antennas and Propagation Magazine, IEEE*, vol. 37, pp. 12 –24, Oct. 1995.

[82] J. Webb, "Hierarchal vector basis functions of arbitrary order for triangular and tetrahedral finite elements," *Antennas and Propagation, IEEE Transactions on*, vol. 47, pp. 1244–1253, Aug 1999.

[83] G. Mur, "Edge elements, their advantages and their disadvantages," *Magnetics, IEEE Transactions on*, vol. 30, pp. 3552–3557, Sep 1994.

[84] R. Otin, "Regularized Maxwell equations and nodal finite elements for electromagnetic field computations," *Electromagnetics*, vol. 30, pp. 190–204, 2010.

[85] M. Costabel and M. Dauge, "Weighted regularization of Maxwell equations in polyhedral domains," *Numerische Mathematik*, vol. 93, pp. 239–277, 2002. 10.1007/s002110100388.

[86] T. Warburton and M. Embree, "The role of the penalty in the local discontinuous Galerkin method for Maxwell's eigenvalue problem," *Computer Methods in Applied Mechanics and Engineering*, vol. 195, no. 25–28, pp. 3205 – 3223, 2006. Discontinuous Galerkin Methods.

[87] G. Cohen and M. Duruflé, "Non-Spurious Spectral Like Element Methods for Maxwell's equations," *Journal of Computational Mathematics*, pp. 282–304, 2007.

[88] G. Cohen, X. Ferrieres, and S. Pernet, "A spatial high-order hexahedral discontinuous Galerkin method to solve Maxwell's equations in time domain," *Journal of Computational Physics*, vol. 217, no. 2, pp. 340 – 363, 2006.

[89] *The Discontinuous Galerkin Finite Element Time Domain Method (DGFETD): A High Order, Globally-Explicit Method for Parallel Computation*, 2007.

[90] S. Piperno, "Symplectic local time-stepping in non-dissipative DGTD methods applied to wave propagation problems," *ESAIM: Mathematical Modelling and Numerical Analysis*, vol. 40, pp. 815–841, 1 2007.

[91] A. Bossavit, "A rationale for edge-elements in 3-D fields computations," *Magnetics, IEEE Transactions on*, vol. 24, no. 1, pp. 74–79, 1988.

[92] J. Nedelec, "Mixed finite elements in R3," *Numerische Mathematik*, vol. 35, no. 3, pp. 315–341, 1980.

[93] J. Nedelec, "A new family of mixed finite elements in R3," *Numerische Mathematik*, vol. 50, no. 1, pp. 57–81, 1986.

[94] G. Mur, "The fallacy of edge elements," *Magnetics, IEEE Transactions on*, vol. 34, pp. 3244–3247, Sep 1998.

[95] J. Hesthaven, "From electrostatics to almost optimal nodal sets for polynomial interpolation in a simplex," *SIAM J. Numer. Anal*, vol. 35, pp. 655–676, 1998.

[96] S. Chun and J. Hesthaven, "High-order accurate thin layer approximations for time-domain electromagnetics. part i: General metal backed coatings," *Journal of Computational and Applied Mathematics*, vol. 231, no. 2, pp. 598 – 611, 2009.

[97] H. Fahs, "Recent achievements on a non-conforming DGTD method for time-domain electromagnetics," 2009.

[98] H. Fahs, "Improving accuracy of high-order discontinuous Galerkin method for time-domain electromagnetics on curvilinear domains," *International Journal of Computer Mathematics*, vol. 88, no. 10, pp. 2124–2153, 2011.

[99] T. Warburton, "A low storage curvilinear discontinuous Galerkin time-domain method for electromagnetics," in *Electromagnetic Theory (EMTS), 2010 URSI International Symposium on*, pp. 996–999, Aug 2010.

[100] "Gmsh, a three-dimensional finite element mesh generator with built-in pre- and post-processing facilities." http://geuz.org/gmsh/.

[101] "GiD the personal pre and post processor." http://www.gidhome.com/.

[102] P. olof Persson and J. Peraire, "Curved mesh generation and mesh refinement using lagrangian solid mechanics," 2012.

[103] P. Silvester, "Symmetric quadrature formulae for simplexes," *Mathematics of Computation*, vol. 24, pp. 95–95, 1970.

[104] H. Fahs, "High-order leap-frog based discontinuous Galerkin method for the time-domain Maxwell equations on non-conforming simplicial meshes," *Numerical Mathematics: A Journal of Chinese Universities*, vol. 2, pp. 275 – 300, Aug. 2009.

[105] S. Dosopoulos, B. Zhao, and J.-F. Lee, "Non-conformal and parallel discontinuous Galerkin time domain method for Maxwell's equations: EM analysis of IC packages," *Journal of Computational Physics*, vol. 238, no. 0, pp. 48 – 70, 2013.

[106] C. Durochat, S. Lanteri, and C. Scheid, "High order non-conforming multi-element discontinuous Galerkin method for time domain electromagnetics," *Applied Mathematics and Computation*, vol. 224, pp. 681–704, Nov. 2013.

[107] R. Leger, J. Viquerat, C. Durochat, C. Scheid, and S. Lanteri, "A parallel non-confoming multi-element DGTD method for the simulation of electromagnetic wave interaction with metallic nanoparticles," *Journal of Computational and Applied Mathematics*, no. 0, pp. –, 2013.

[108] M. Bergot and M. Duruflé, "Higher-order discontinuous Galerkin method for pyramidal elements using orthogonal bases," *Numerical Methods for Partial Differential Equations*, vol. 29, no. 1, pp. 144–169, 2013.

[109] M. Bergot, *Elements finis d dordre eleve pour maillages hybrides*. PhD thesis, Universite Paris Daphine, 2012.

[110] L. Shampine, "Stability of the leapfrog/midpoint method," *Applied Mathematics and Computation*, vol. 208, no. 1, pp. 293–298, 2009.

[111] R. Diehl, K. Busch, and J. Niegemann, "Comparison of low-storage Runge-Kutta schemes for discontinuous Galerkin time-domain simulations of Maxwell's equations," *Journal of Computational and Theoretical Nanoscience*, vol. 7, no. 8, pp. 1572–1580, 2010.

[112] J. Niegemann, R. Diehl, and K. Busch, "Efficient low-storage Runge–Kutta schemes with optimized stability regions," *Journal of Computational Physics*, vol. 231, no. 2, pp. 364 – 372, 2012.

[113] B. Cockburn and C.-W. Shu, "Runge–Kutta discontinuous Galerkin methods for convection-dominated problems," *Journal of scientific computing*, vol. 16, no. 3, pp. 173–261, 2001.

[114] M. Lilienthal, S. M. Schnepp, and T. Weiland, "Non-dissipative space-time *hp*-discontinuous Galerkin method for the time-dependent Maxwell equations," *ArXiv e-prints*, July.

[115] R. Griesmaier and P. Monk, "Discretization of the wave equation using continuous elements in time and a hybridizable discontinuous Galerkin method in space," *Journal of Scientific Computing*, pp. 1–27, 2013.

[116] M. J. Grote, M. Mehlin, and T. Mitkova, "Runge-Kutta based explicit local time-stepping methods for wave propagation," in *Scientific Computing in Electrical Engineering*, 2014.

[117] P. Monk and G. R. Richter, "A discontinuous Galerkin method for linear symmetric hyperbolic systems in inhomogeneous media," *Journal of Scientific Computing*, vol. 22-23, pp. 443–477, 2005.

[118] V. Dolean, H. Fahs, L. Fezoui, and S. Lanteri, "Locally implicit discontinuous Galerkin method for time domain electromagnetics," *J. Comput. Phys.*, vol. 229, pp. 512–526, Jan. 2010.

[119] A. Kanevsky, M. H. Carpenter, D. Gottlieb, and J. S. Hesthaven, "Application of implicit-explicit high order Runge-Kutta methods to discontinuous-Galerkin schemes," *Journal of Computational Physics*, vol. 225, no. 2, pp. 1753 – 1781, 2007.

[120] S. Dosopoulos, *Interior Penalty Discontinuous Galerkin Finite Element Method for the Time-Domain Maxwell's Equations*. PhD thesis, Ohio State University, 2012.

[121] J. H. Wilkinson, *The Algebraic Eigenvalue Problem*. Clarendon Press, 1964.

[122] L. Fezoui, S. Lanteri, S. Lohrengel, and S. Piperno, "Convergence and stability of a discontinuous Galerkin time-domain method for the 3D heterogeneous Maxwell equations on unstructured meshes," *ESAIM: Mathematical Modelling and Numerical Analysis*, vol. 39, pp. 1149–1176, 11 2005.

[123] D. Sarmany, M. Botchev, and J. van der Vegt, "Time-integration methods for finite element discretisations of the second-order Maxwell equation," *Computers & Mathematics with Applications*, vol. 65, no. 3, pp. 528 – 543, 2013.

[124] J. H. Williamson, "Low-storage Runge-Kutta schemes," *Journal of Computational Physics*, vol. 35, no. 1, pp. 48 – 56, 1980.

[125] C. A. Kennedy, M. H. Carpenter, and R. M. Lewis, "Low-storage, explicit Runge-Kutta schemes for the compressible Navier-Stokes equations," *Appl. Numer. Math.*, vol. 35, pp. 177–219, November 2000.

[126] C. Chauviere, J. Hesthaven, A. Kanevsky, and T. Warburton, "High-order localized time integration for grid-induced stiffness," in *Computational Fluid and Solid Mechanics 2003* (K. Bathe, ed.), pp. 1883 – 1886, Oxford: Elsevier Science Ltd, 2003.

[127] A. Taube, M. Dumbser, C.-D. Munz, and R. Schneider, "A high-order discontinuous Galerkin method with time-accurate local time stepping for the Maxwell equations," *International Journal of Numerical Modelling: Electronic Networks, Devices and Fields*, vol. 22, no. 1, pp. 77–103, 2009.

[128] M. Liu, K. Sirenko, and H. Bagci, "An efficient discontinuous Galerkin finite element method for highly accurate solution of Maxwell equations," *Antennas and Propagation, IEEE Transactions on*, vol. 60, no. 8, pp. 3992–3998, 2012.

[129] A. Glaser and V. Rokhlin, "A new class of highly accurate solvers for ordinary differential equations," *Journal of Scientific Computing*, vol. 38, no. 3, pp. 368–399, 2009.

[130] R. S. Falk and G. R. Richter, "Explicit finite element methods for symmetric hyperbolic equations," *SIAM J. Numer. Anal.*, vol. 36, pp. 935–952, Mar. 1999.

[131] F. Kretzschmar, S. M. Schnepp, I. Tsukerman, and T. Weiland, "Discontinuous Galerkin methods with trefftz approximation," *arXiv (submitted)*, 2013.

[132] S. C. H. Allen Taflove, *Computational Electrodynamics The Finite-Differences Time Domain Method*. British Library, 2000.

[133] D. Merewether, R. Fisher, and F. Smith, "On implementing a numeric Huygen's source scheme in a finite difference program to illuminate scattering bodies," *Nuclear Science, IEEE Transactions on*, vol. 27, pp. 1829–1833, Dec 1980.

[134] R. Luebbers, K. Kunz, M. Schneider, and F. Hunsberger, "A finite-difference time-domain near zone to far zone transformation [electromagnetic scattering]," *Antennas and Propagation, IEEE Transactions on*, vol. 39, pp. 429 –433, apr 1991.

[135] "Higher-order time-domain methods for the analysis of nano-photonic systems," *Photonics and Nanostructures - Fundamentals and Applications*, vol. 7, no. 1, pp. 2 – 11, 2009.

[136] R. Gomez Martin, *Electromagnetic field theory for physicist and engineers: Fundamentals and Applications*. Grupo de Electromagnetismo de Granada, 2006.

[137] M. Abramowitz and I. A. Stegun, *Handbook of Mathematical Functions: with Formulas, Graphs, and Mathematical Tables*. Dover books on mathematics, New York: Dover, June 1972.

[138] J.-P. Berenger, "A perfectly matched layer for the absorption of electromagnetic waves," *Journal of Computational Physics*, vol. 114, pp. 185–200, 1994.

[139] S. Gedney and B. Zhao, "An auxiliary differential equation formulation for the complex-frequency shifted PML," *Antennas and Propagation, IEEE Transactions on*, vol. 58, no. 3, pp. 838 –847, 2010.

[140] S. D. Gedney, "An anisotropic perfectly matched layer-absorbing medium for the truncation of FDTD lattices," *Antennas and Propagation, IEEE Transactions on*, vol. 44, no. 12, pp. 1630–1639, 1996.

[141] S. G. Garcia, I. V. Pérez, R. G. Martin, and B. G. Olmedo, "Applicability of the PML absorbing boundary condition to dielectric anisotropic media," *Electronics Letters*, vol. 32, no. 14, pp. 1270–1271, 1996.

[142] S. G. Garcia, I. V. Perez, R. G. Martin, and B. G. Olmedo, "BiPML: A PML to match waves in bianisotropic media," *Microwave and Optical Technology Letters*, vol. 20, no. 1, pp. 44–48, 1999.

[143] M. Gribbons, A. Pinello, and A. Cangellaris, "A stretched coordinate technique for numerical absorption of evanescent and propagating waves in planar waveguiding structures," *Microwave Theory and Techniques, IEEE Transactions on*, vol. 43, pp. 2883 –2889, Dec. 1995.

[144] F. L. Teixeira and W. C. Chew, "Analytical derivation of a conformal perfectly matched absorber for electromagnetic waves," *Microwave and Optical Technology Letters*, vol. 17, no. 4, pp. 231–236, 1998.

[145] J. A. Roden and S. D. Gedney, "Convolution PML (CPML): An efficient FDTD implementation of the CFS–PML for arbitrary media," *Microwave and Optical Technology Letters*, vol. 27, no. 5, pp. 334–339, 2000.

[146] F. Teixeira, K.-P. Hwang, W. Chew, and J.-M. Jin, "Conformal PML-FDTD schemes for electromagnetic field simulations: a dynamic stability study," *Antennas and Propagation, IEEE Transactions on*, vol. 49, pp. 902 –907, June 2001.

[147] M. Kuzuoglu and R. Mittra, "Frequency dependence of the constitutive parameters of causal perfectly matched anisotropic absorbers," *Microwave and Guided Wave Letters, IEEE*, vol. 6, no. 12, pp. 447–449, 1996.

[148] F. Teixeira and W. Chew, "Extension of the PML absorbing boundary condition to 3D spherical coordinates: scalar case," *Magnetics, IEEE Transactions on*, vol. 34, pp. 2680 –2683, Sept. 1998.

[149] C. H. Wilcox, "An expansion theorem for electromagnetic fields," *Communications on Pure and Applied Mathematics*, vol. 9, no. 2, pp. 115–134, 1956.

[150] J. A. Stratton, *Electromagnetic theory*. McGraw-Hill New York, 1st ed. ed., 1941.

[151] S. Garcia, R. Rubio, A. Bretones, and R. Martin, "Extension of the ADI-FDTD method to Debye media," *Antennas and Propagation, IEEE Transactions on*, vol. 51, pp. 3183 – 3185, nov. 2003.

[152] C. Scheid and S. Lanteri, "Convergence of a discontinuous Galerkin scheme for the mixed time domain Maxwell's equations in dispersive media.," Research Report RR-7634, INRIA, May 2011.

[153] J. Viquerat, K. Maciej, S. Lantéri, and C. Scheid, "Theoretical and numerical analysis of local dispersion models coupled to a discontinuous Galerkin time-domain method for Maxwell's equations," Rapport de recherche RR-8298, INRIA, May 2013. MIBC VF.

[154] S.-C. Kong, J. Simpson, and V. Backman, "ADE-FDTD scattered-field formulation for dispersive materials," *IEEE Microwave and Wireless Components Letters*, vol. 18, p. 1, 2008.

[155] X. Ji, W. Cai, and P. Zhang, "High-order DGTD methods for dispersive Maxwell's equations and modelling of silver nanowire coupling," *International Journal for Numerical Methods in Engineering*, vol. 69, no. 2, pp. 308–325, 2007.

[156] S. D. Gedney, J. C. Young, T. C. Kramer, and J. Roden, "A discontinuous Galerkin finite element time-domain method modeling of dispersive media," *Antennas and Propagation, IEEE Transactions on*, vol. 60, no. 4, pp. 1969–1977, 2012.

[157] H. Banks, V. Bokil, and N. Gibson, "Analysis of stability and dispersion in a finite element method for Debye and Lorentz dispersive media," *Numerical Methods for Partial Differential Equations*, vol. 25, no. 4, pp. 885–917, 2009.

[158] B. Wang, Z. Xie, and Z. Zhang, "Error analysis of a discontinuous Galerkin method for Maxwell equations in dispersive media," *Journal of Computational Physics*, vol. 229, no. 22, pp. 8552 – 8563, 2010.

[159] M. Han, R. Dutton, and S. Fan, "Model dispersive media in finite-difference time-domain method with complex-conjugate pole-residue pairs," *Microwave and Wireless Components Letters, IEEE*, vol. 16, no. 3, pp. 119 –121, 2006.

[160] H. Lin, M. F. Pantoja, L. D. Angulo, J. Alvarez, R. G. Martin, and S. G. Garcia, "FDTD modeling of graphene devices using complex conjugate dispersion material model," *Microwave and Wireless Components Letters, IEEE*, vol. 22, pp. 612 –614, dec. 2012.

[161] D. Deschrijver, M. Mrozowski, T. Dhaene, and D. l. De Zutter, "Macromodeling of multiport systems using a fast implementation of the vector fitting method," *IEEE Microwave and Wireless Components Letters*, vol. 18, no. 6, pp. 383–385, 2008.

[162] B. Gustavsen, "Improving the pole relocating properties of vector fitting," *IEEE Trans. Power Delivery*, vol. 21, pp. 1587–1592, July 2006.

[163] B. Gustavsen and A. Semlyen, "Rational approximation of frequency domain responses by vector fitting," *Power Delivery, IEEE Transactions on*, vol. 14, pp. 1052 –1061, jul 1999.

[164] F. Q. Hu, M. Y. Hussaini, and P. Rasetarinera, "An analysis of the discontinuous Galerkin method for wave propagation problems," *Journal of Computational Physics*, vol. 151, no. 2, pp. 921 – 946, 1999.

[165] J. Li, "Unified analysis of leap-frog methods for solving time-domain Maxwell's equations in dispersive media," *J. Sci. Comput.*, vol. 47, pp. 1–26, April 2011.

[166] M. Konig, K. Busch, and J. Niegemann, "The discontinuous Galerkin time-domain method for Maxwell's equations with anisotropic materials," *Photonics and Nanostructures - Fundamentals and Applications*, vol. 8, no. 4, pp. 303 – 309, 2010. Tacona Photonics 2009.

[167] X.-Q. Sheng and z. peng, "Analysis of scattering by large objects with off-diagonally anisotropic material using finite element-boundary integral-multilevel fast multipole algorithm," *Microwaves, Antennas Propagation, IET*, vol. 4, pp. 492–500, April 2010.

[168] S. Dosopoulos and J.-F. Lee, "Interconnect and lumped elements modeling in interior penalty discontinuous Galerkin time-domain methods," *Journal of Computational Physics*, vol. 229, no. 22, pp. 8521 – 8536, 2010.

[169] B. Zhao, *The application of Discontinuous Galerkin Finite Element Time-Domain Method in the design, simulation and analysis of modern radio frequency systems*. PhD thesis, University of Kentucky Doctoral Dissertations, 2011.

[170] B. Zhao, J. Young, and S. Gedney, "SPICE lumped circuit subcell model for the discontinuous Galerkin finite-element time-domain method," *Microwave Theory and Techniques, IEEE Transactions on*, vol. 60, pp. 2684 –2692, sept. 2012.

[171] L. Li, S. Lanteri, and R. Perrussel, "A hybridizable discontinuous Galerkin method for solving 3D time-harmonic Maxwells equations," in *Numerical Mathematics and Advanced Applications 2011* (A. Cangiani, R. L. Davidchack, E. Georgoulis, A. N. Gorban, J. Levesley, and M. V. Tretyakov, eds.), pp. 119–128, Springer Berlin Heidelberg, 2013.

[172] M. Sarto, "A new model for the FDTD analysis of the shielding performances of thin composite structures," *Electromagnetic Compatibility, IEEE Transactions on*, vol. 41, pp. 298 –306, Nov. 1999.

[173] C. L. Holloway, M. S. Sarto, and M. Johansson, "Analyzing carbon-fiber composite materials with equivalent-layer models," *Electromagnetic Compatibility, IEEE Transactions on*, vol. 47, no. 4, pp. 833–844, 2005.

[174] L. D. Angulo, S. Greco, M. Ruiz-Cabello, S. G. Garcia, and M. S. Sarto, "FDTD techniques to simulate composite air vehicles for EM," in *AES Symposium, Paris*, 2012.

[175] S. Chun, H. Haddar, and J. Hesthaven, "High-order accurate thin layer approximations for time-domain electromagnetics, part ii: Transmission layers," *Journal of Computational and Applied Mathematics*, vol. 234, no. 8, pp. 2587 – 2608, 2010.

[176] D. Pozar, *Microwave Engineering, 3Rd Ed*. Wiley India Pvt. Limited, 2009.

[177] R. Holland and L. Simpson, "Finite-difference analysis of EMP coupling to thin struts and wires," *Electromagnetic Compatibility, IEEE Transactions on*, vol. EMC-23, pp. 88 –97, may 1981.

[178] F. Edelvik and T. Weiland, "Stable modelling of arbitrary thin slots in the finite-element time-domain method," *International Journal of Numerical Modelling: Electronic Networks, Devices and Fields*, vol. 17, no. 4, pp. 365–383, 2004.

[179] S. Gao, Q. Cao, J. Ding, M. Zhu, and Y. Lu, "A hybrid DGTD-TDIE method for solving complex electromagnetic problems," *Journal of Electromagnetic Waves and Applications*, vol. 27, no. 8, pp. 1017–1027, 2013.

[180] "OpenFOAM, the open source CFD toolbox." http://www.openfoam.com/.
[181] F.-G. Hu and C.-F. Wang, "Parallel higher-order DG-FETD simulation of antennas (invited paper)," in *Antennas Propagation (ISAP), 2013 Proceedings of the International Symposium on*, vol. 01, pp. 71–72, Oct 2013.
[182] A. Klockner, T. Warburton, J. Bridge, and J. S. Hesthaven, "Nodal discontinuous Galerkin methods on graphics processors," *J. Comput. Phys.*, vol. 228, pp. 7863–7882, November 2009.
[183] A. Klockner, T. Warburton, and J. Hesthaven, "High-order discontinuous Galerkin methods by GPU metaprogramming," in *GPU Solutions to Multi-scale Problems in Science and Engineering* (D. A. Yuen, L. Wang, X. Chi, L. Johnsson, W. Ge, and Y. Shi, eds.), Lecture Notes in Earth System Sciences, pp. 353–374, Springer Berlin Heidelberg, 2013.
[184] "ParMETIS, parallel graph partitioning and fill-reducing matrix ordering." http://glaros.dtc.umn.edu/gkhome/metis/parmetis/overview.
[185] L. Mattes and S. Kofuji, "The use of overlapping subgrids to accelerate the FDTD on GPU devices," in *Radar Conference, 2010 IEEE*, pp. 807–810, May 2010.